
Hyperbolic Neural Networks++

Ryohei Shimizu¹, Yusuke Mukuta^{1,2}, Tatsuya Harada^{1,2}

¹The University of Tokyo

²RIKEN AIP

{shimizu, mukuta, harada}@mi.t.u-tokyo.ac.jp

Abstract

Hyperbolic spaces, which have the capacity to embed tree structures without distortion owing to their exponential volume growth, have recently been applied to machine learning to better capture the hierarchical nature of data. In this study, we reconsider a way to generalize the fundamental components of neural networks in a single hyperbolic geometry model, and propose novel methodologies to construct a multinomial logistic regression, fully-connected layers, convolutional layers, and attention mechanisms under a unified mathematical interpretation, without increasing the parameters. A series of experiments show the parameter efficiency of our methods compared to a conventional hyperbolic component, and stability and outperformance over their Euclidean counterparts.

1 Introduction

Shifting the arithmetic stage of a neural network to a non-Euclidean geometry such as a hyperbolic space is a promising way to find more suitable geometric structures for representing or processing data. Owing to its exponential growth in volume with respect to its radius [17, 16], a hyperbolic space has the capacity to continuously embed tree structures with an arbitrarily low distortion [16, 36], and has been directly utilized, for instance, to visualize large taxonomic graphs [18], to embed scale-free graphs [4], or to learn hierarchical lexical entailments [30]. Compared to a flat Euclidean geometry, a hyperbolic space shows a higher embedding accuracy under fewer dimensions in such cases.

Because a wide variety of real-world data encompasses some type of latent hierarchical structures [14, 28, 22, 16], it has been empirically proven that a hyperbolic space is able to capture such intrinsic features thorough representation learning [16, 8, 29, 39, 19, 2, 11]. Motivated by such expressive characteristics, various machine learning methods, including support vector machines [7] and neural networks [9, 12, 25, 27, 6] have derived the analogous benefits from the introduction of a hyperbolic space, with an aim to improve the performance on advanced tasks beyond just representing data.

One of the pioneering approaches is Hyperbolic Neural Networks (HNNs), which introduced an easy-to-interpret and highly analytical coordinate system of hyperbolic spaces, namely, the Poincaré ball model, with a corresponding gyrovector space to smoothly connect the fundamental functions common to neural networks into valid ones in a hyperbolic geometry [9]. Built upon the solid foundation of HNNs, the essential components for neural networks covering the multinomial logistic regression (MLR), fully-connected (FC) layers, and Recurrent Neural Networks have been realized in the Poincaré ball model. In addition to the formalism, the methods for graphs [23], sequential classification [25], or Variational Autoencoders [27, 24, 32, 37] are further constructed. Such studies have applied the Poincaré ball model as a natural and viable option in the area of deep learning.

Despite such progress, however, unsolved problems and uncovered regions remain. In terms of the network architectures, the current formulation of hyperbolic MLR requires almost twice the number of parameters compared to its Euclidean counterpart, which makes it unscalable in cases in which numerous embedded entities should be classified or where large hidden dimensions are employed,

such as in natural language processing. The lack of convolutional layers must also be mentioned, because their application is now ubiquitous and is no longer limited to the field of computer vision.

Diving deep into the individual functions, the split and concatenation of vectors have yet to be realized in a hyperbolic space in a manner that can fully exploit such space and allow sub-vectors to achieve a commutative property. In addition, a closed-form centroid also remains unclear. Although one type of hyperbolic geometry model has a midpoint definition, called the Einstein midpoint [45], and another centroid formulation has been shown in a subsequent study [19], neither method has been applied to the Poincaré ball model, nor have their geometric relationships been analyzed. Because isomorphic conversions exist between different models, one can switch models prior to operation and restore them afterward. However, the fact that such a basic component cannot be utilized with mathematical consistency is a fatal flaw, particularly in the efficient building of a modern attention scheme.

Based on the above, we reconsider the flow of several extensions to bridge Euclidean operations into hyperbolic operations and construct alternative or novel methods on the Poincaré ball model. Specifically, the main contributions of this paper are summarized as follows:

1. We reformulate a hyperbolic MLR to reduce the required parameters to the same level as a Euclidean version while maintaining the same range of representational properties.
2. We further exploit this knowledge as a replacement of an affine transformation in the FC layers, and propose a novel generalization that can more properly utilize the hyperbolic nature compared with a previous method [9].
3. We generalize the split and concatenation of coordinates to the Poincaré ball model by setting the invariance of the expected value of the vector norm as a criterion.
4. By combining the contributions 2, 3, we further define a novel generalization scheme of arbitrary dimensional convolutional layers in the Poincaré ball model.
5. We derive the Poincaré weighted centroid as a minimizer of the squared Lorentzian distances [19], and associate it with the Möbius coaddition and the Einstein midpoint.
6. Integrating all previous contributions 1, 2, 3, 5, we construct a completely hyperbolic multi-head attention mechanism realized in the Poincaré ball model.

We experimentally demonstrate the effectiveness of our methods over conventional HNNs based on a performance test of MLR functions, and their higher stability and performance than Euclidean equivalents in experiments with Set Transformers [21] and convolutional sequence to sequence [10].

2 Hyperbolic Geometry

Hyperbolic spaces are Riemannian manifolds with a constant negative curvature. In this section, we briefly review a Riemannian geometry and two isometric models of a hyperbolic geometry.

Riemannian geometry. An n -dimensional manifold \mathcal{M} is an n -dimensional topological space that can be linearly approximated to an n -dimensional real space at an arbitrary point $x \in \mathcal{M}$, and each local linear space is called a tangent space $\mathcal{T}_x\mathcal{M}$. A Riemannian manifold is a pairing of a differentiable manifold and a metric tensor field \mathbf{g} as a function of each point x , which is expressed as $(\mathcal{M}, \mathbf{g})$. Here, \mathbf{g} defines an inner product on each tangent space such that $\forall \mathbf{u}, \mathbf{v} \in \mathcal{T}_x\mathcal{M}, \langle \mathbf{u}, \mathbf{v} \rangle_x = \mathbf{u}^\top \mathbf{g}_x \mathbf{v}$, where \mathbf{g}_x is a positive definite symmetric matrix defined on $\mathcal{T}_x\mathcal{M}$. The norm of a tangent vector derived from the inner product is defined as $\|\mathbf{v}\|_x = \sqrt{|\langle \mathbf{v}, \mathbf{v} \rangle_x|}$. A metric tensor \mathbf{g}_x provides local information regarding the angle between, and the length of, the tangent vectors in $\mathcal{T}_x\mathcal{M}$, which induces the global length of the curves on \mathcal{M} through an integration. In particular, the shortest path connecting two arbitrary points on \mathcal{M} at a constant speed is called a geodesic, the length of which becomes the distance. Along a geodesic where one of the endpoints is x , the function projecting a tangent vector $\mathbf{v} \in \mathcal{T}_x\mathcal{M}$ as an initial velocity vector onto \mathcal{M} is denoted as an exponential map $\exp_x(\mathbf{v})$, and its inverse function is called a logarithmic map $\log_x = \exp_x^{-1}$. In addition, the concept of parallel transport $P_{x \rightarrow y} : \mathcal{T}_x\mathcal{M} \rightarrow \mathcal{T}_y\mathcal{M}$ is generalized to the specially conditioned unique linear isometry between two tangent spaces. For more details, refer to [38, 35, 1].

Note that, in this study, we equate \mathbf{g} with \mathbf{g}_x if \mathbf{g}_x is constant, and denote the Euclidean inner product, norm, and unit vector for any real vector $\mathbf{u}, \mathbf{v} \in \mathbb{R}^n$ as $\langle \mathbf{u}, \mathbf{v} \rangle$, $\|\mathbf{v}\|$, and $[\mathbf{v}] = \mathbf{v}/\|\mathbf{v}\|$, respectively.

Hyperboloid model. The n -dimensional hyperboloid model is a hypersurface in an $(n + 1)$ -dimensional Minkowski space \mathbb{R}_1^{n+1} equipped with an inner product $\langle \mathbf{x}, \mathbf{y} \rangle_{\mathcal{L}} = \mathbf{x}^\top \mathbf{g}_{\mathcal{L}} \mathbf{y}$ for $\forall \mathbf{x}, \mathbf{y} \in \mathbb{R}_1^{n+1}$, where $\mathbf{g}_{\mathcal{L}} = \text{diag}(-1, \mathbf{1}_n^\top)$. Given a constant negative curvature $-c$, the model is then defined by $(\mathbb{H}_c^n, \mathbf{g}_{\mathcal{L}})$, where $\mathbb{H}_c^n = \{\mathbf{x} = (x_0, \dots, x_n)^\top \in \mathbb{R}_1^{n+1} \mid c\langle \mathbf{x}, \mathbf{x} \rangle_{\mathcal{L}} = -1, x_0 > 0\}$.

Poincaré ball model. The n -dimensional Poincaré ball model of a constant negative curvature $-c$ is defined by $(\mathbb{B}_c^n, \mathbf{g}^c)$, where $\mathbb{B}_c^n = \{\mathbf{x} \in \mathbb{R}^n \mid c\|\mathbf{x}\|^2 < 1\}$ and $\mathbf{g}_x^c = (\lambda_x^c)^2 \mathbf{I}_n$. Here, \mathbb{B}_c^n is an open ball of radius $1/\sqrt{c}$, and $\lambda_x^c = 2(1 - c\|\mathbf{x}\|^2)^{-1}$ is a conformal factor, which induces the inner product $\langle \mathbf{u}, \mathbf{v} \rangle_x^c = (\lambda_x^c)^2 \langle \mathbf{u}, \mathbf{v} \rangle$ and norm $\|\mathbf{v}\|_x^c = \lambda_x^c \|\mathbf{v}\|$ for $\mathbf{u}, \mathbf{v} \in \mathcal{T}_x \mathbb{B}_c^n$. The exponential, logarithmic maps and parallel transport are denoted as \exp_x^c , \log_x^c and $P_{x \rightarrow y}^c$, respectively, as shown in Appendix B.

To operate the coordinates in the Poincaré ball model as vector-like mathematical objects, the Möbius gyrovector space provides a special algebra that treats them as gyrovectors, equipped with various operations including the generalized vector addition, that is, a noncommutative and nonassociative binary operation called the Möbius addition \oplus_c , and its variant of subtraction \ominus_c [45]. They converge to the ordinary $+$ and $-$ in the limit $c \rightarrow 0$, respectively, in connection with the Euclidean geometry, the curvature of which is zero. For their definitions and closed-form expressions, see Appendix A.

Poincaré hyperplane. The notion of a hyperplane is generalized to a Poincaré hyperplane $\tilde{H}_{a,p}^c$ in [9], which is the set of all geodesics containing an arbitrary point $\mathbf{p} \in \mathbb{B}_c^n$ and orthogonal to an arbitrary tangent vector $\mathbf{a} \in \mathcal{T}_{\mathbf{p}} \mathbb{B}_c^n$. As shown in Appendix B.2, [9] also extends the distance d_c between two points in \mathbb{B}_c^n into one from a point in \mathbb{B}_c^n to a Poincaré hyperplane in a closed form.

Isometric isomorphism. The bijection between an arbitrary point $\mathbf{h} = (z, \mathbf{k}^\top)^\top \in \mathbb{H}_c^n$ and its unique corresponding point $\mathbf{b} \in \mathbb{B}_c^n$, depicted in Figure 1, is given by the following:

$$\mathbb{H}_c^n \rightarrow \mathbb{B}_c^n : \mathbf{b} = \frac{\mathbf{k}}{1 + \sqrt{cz}}, \quad \mathbb{B}_c^n \rightarrow \mathbb{H}_c^n : z = \frac{1}{\sqrt{c}} \frac{1 + c\|\mathbf{b}\|^2}{1 - c\|\mathbf{b}\|^2}, \quad \mathbf{k} = \frac{2\mathbf{b}}{1 - c\|\mathbf{b}\|^2}. \quad (1)$$

3 Hyperbolic Neural Networks++

Aiming to overcome the difficulties discussed in Section 1, we build the novel scheme of hyperbolic neural networks in the Poincaré ball model. The core concept is the regeneration of $\langle \mathbf{a}, \mathbf{x} \rangle - b$ type equations with no increase in the number of parameters, which has the potential to replace any affine transformation in a shared manner. Specifically, this section starts from the reformulation of the hyperbolic MLR, from which the variants to the FC, convolutional, and multi-head attention layers are derived. Several other modifications are also proposed to support neural networks with broad architectures.

3.1 Unidirectional reparameterization of hyperbolic multinomial logistic regression

Given an input $\mathbf{x} \in \mathbb{R}^n$, MLR is an operation used to predict the probabilities of all target outcomes $k \in \{1, 2, \dots, K\}$ for the objective variable y as a log-linear model and is described as follows:

$$p(y = k \mid \mathbf{x}) \propto \exp(v_k(\mathbf{x})), \quad \text{where } v_k(\mathbf{x}) = \langle \mathbf{a}_k, \mathbf{x} \rangle - b_k, \quad \mathbf{a}_k \in \mathbb{R}^n, \quad b_k \in \mathbb{R}. \quad (2)$$

Circumvention of the double vectorization. To generalize the score function v_k to the Poincaré ball model, [9] has first re-parameterized the scalar term b_k as a vector $\mathbf{p}_k \in \mathbb{R}^n$ in the form $\langle \mathbf{a}_k, \mathbf{x} \rangle - b_k = \langle \mathbf{a}_k, -\mathbf{p}_k + \mathbf{x} \rangle$, where $b_k = \langle \mathbf{a}_k, \mathbf{p}_k \rangle$. However, this causes an undesirable increase

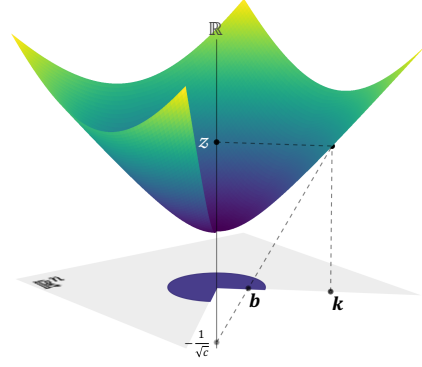
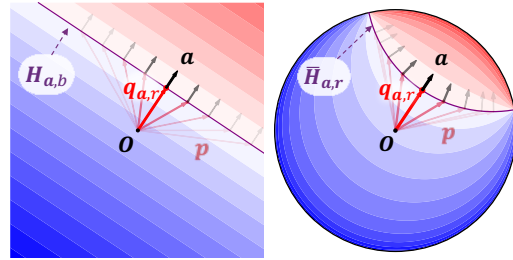


Figure 1: Geometric relationship between \mathbb{H}_c^n and \mathbb{B}_c^n depicted in \mathbb{R}_1^{n+1} .



(a) Reformulation in \mathbb{R}^n (b) Generalization to \mathbb{B}_c^n

Figure 2: Whichever pair of \mathbf{a} and \mathbf{p} is chosen, a determined discriminative hyperplane is the same. Considering one bias point $\mathbf{q}_{a,r}$ per one discriminative hyperplane solves this over-parameterization.

in the parameters from $n + 1$ to $2n$ in each class k . As illustrated in Figure 2 (a), this reformulation is redundant from the viewpoint that there exist countless choices of \mathbf{p}_k to determine the same discriminative hyperplane $H_{\mathbf{a}_k, b_k} = \{\mathbf{x} \in \mathbb{R}^n \mid \langle \mathbf{a}_k, \mathbf{x} \rangle - b_k = 0\}$. Because the key of this step is to replace all variables with the same dimensional vectors attributed to the same manifold, we introduce another scalar parameter $r_k \in \mathbb{R}$ instead, which makes the bias vector $\mathbf{q}_{\mathbf{a}_k, r_k}$ parallel to \mathbf{a}_k :

$$\langle \mathbf{a}_k, \mathbf{x} \rangle - b_k = \langle \mathbf{a}_k, -\mathbf{q}_{\mathbf{a}_k, r_k} + \mathbf{x} \rangle, \text{ where } \mathbf{q}_{\mathbf{a}_k, r_k} = r_k [\mathbf{a}_k] \text{ s.t. } b_k = r_k \|\mathbf{a}_k\|. \quad (3)$$

One possible realization of \mathbf{p}_k is adopted to reduce the previously mentioned redundancies without a loss of generality or representational properties compared to the original affine transformation, and induces another expression of the hyperplane, $\bar{H}_{\mathbf{a}_k, r_k} := \{\mathbf{x} \in \mathbb{R}^n \mid \langle \mathbf{a}_k, -\mathbf{q}_{\mathbf{a}_k, r_k} + \mathbf{x} \rangle = 0\} = H_{\mathbf{a}_k, r_k \|\mathbf{a}_k\|}$. Based on distance d from a point to the hyperplane, Eq. (3) can be further rewritten as in [20, 9] in the following form: $\langle \mathbf{a}_k, -\mathbf{q}_{\mathbf{a}_k, r_k} + \mathbf{x} \rangle = \text{sign}(\langle \mathbf{a}_k, -\mathbf{q}_{\mathbf{a}_k, r_k} + \mathbf{x} \rangle) d(\mathbf{x}, \bar{H}_{\mathbf{a}_k, r_k}) \|\mathbf{a}_k\|$.

Unidirectional Poincaré MLR. Based on the observation that $\mathbf{q}_{\mathbf{a}_k, r_k}$ starts from the origin and the concept of Poincaré hyperplanes, we can now generalize v_k for \mathbf{x} , $\mathbf{q}_{\mathbf{a}_k, r_k} \in \mathbb{B}_c^n$ and $\mathbf{a}_k \in \mathcal{T}_{\mathbf{q}_{\mathbf{a}_k, r_k}} \mathbb{B}_c^n$:

$$v_k(\mathbf{x}) = \text{sign}(\langle \mathbf{a}_k, \ominus_c \mathbf{q}_{\mathbf{a}_k, r_k} \oplus_c \mathbf{x} \rangle) d_c(\mathbf{x}, \bar{H}_{\mathbf{a}_k, r_k}^c) \|\mathbf{a}_k\|_{\mathbf{q}_{\mathbf{a}_k, r_k}}^c, \quad (4)$$

$$\text{where } \mathbf{q}_{\mathbf{a}_k, r_k} = \exp_0^c(r_k [\mathbf{a}_k]), \quad \bar{H}_{\mathbf{a}_k, r_k}^c := \{\mathbf{x} \in \mathbb{B}_c^n \mid \langle \mathbf{a}_k, \ominus_c \mathbf{q}_{\mathbf{a}_k, r_k} \oplus_c \mathbf{x} \rangle = 0\}, \quad (5)$$

which are shown in Figure 2 (b). Importantly, the circular reference between $\mathbf{a}_k \in \mathcal{T}_{\mathbf{q}_{\mathbf{a}_k, r_k}} \mathbb{B}_c^n$ and $\mathbf{q}_{\mathbf{a}_k, r_k}$ can be unraveled by considering the tangent vector at the origin, $\mathbf{z}_k \in \mathcal{T}_0 \mathbb{B}_c^n$, from which \mathbf{a}_k is parallel transported by $P_{\mathbf{x} \rightarrow \mathbf{y}}^c : \mathcal{T}_{\mathbf{x}} \mathbb{B}_c^n \rightarrow \mathcal{T}_{\mathbf{y}} \mathbb{B}_c^n$ described in Appendix B.3 as follows:

$$\mathbf{a}_k = P_{\mathbf{0} \rightarrow \mathbf{q}_{\mathbf{a}_k, r_k}}^c(\mathbf{z}_k) = \text{sech}^2(\sqrt{c} r_k) \mathbf{z}_k, \quad \mathbf{q}_{\mathbf{a}_k, r_k} = \exp_0^c(r_k [\mathbf{z}_k]) = \mathbf{q}_{\mathbf{z}_k, r_k}. \quad (6)$$

Combining Eqs. (4), (6), (20), we conclude the derivation of the unidirectional re-generalization of MLR, the parameters of which are $r_k \in \mathbb{R}$ and $\mathbf{z}_k \in \mathcal{T}_0 \mathbb{B}_c^n = \mathbb{R}^n$ for each class k :

$$v_k(\mathbf{x}) = \frac{2\|\mathbf{z}_k\|}{\sqrt{c}} \sinh^{-1} \left(\frac{2\sqrt{c} \langle \mathbf{x}, [\mathbf{z}_k] \rangle}{1 - c\|\mathbf{x}\|^2} \cosh(2\sqrt{c} r_k) - \frac{1 + c\|\mathbf{x}\|^2}{1 - c\|\mathbf{x}\|^2} \sinh(2\sqrt{c} r_k) \right). \quad (7)$$

For more detailed deformation, see Appendix C.1. Note that we recover the form of the standard Euclidean MLR in $\lim_{c \rightarrow 0} v_k(\mathbf{x}) = 4(\langle \mathbf{a}_k, \mathbf{x} \rangle - b_k)$, which is proven in Appendix C.2.

3.2 Reformulating fully-connected layers to properly exploit the hyperbolic properties

We next discuss the FC layers, described as a simple affine transformation $\mathbf{y} = \mathbf{A}\mathbf{x} - \mathbf{b}$, in an element-wise manner with respect to the output space as $y_k = \langle \mathbf{a}_k, \mathbf{x} \rangle - b_k$, where $\mathbf{x}, \mathbf{a}_k \in \mathbb{R}^n$ and $b_k \in \mathbb{R}$. This can be interpreted as an operation that linearly transforms the input \mathbf{x} and treats the output score y_k as the coordinate value at, or the signed distance from the hyperplane containing the origin and orthogonal to, the k -th axis of the output space \mathbb{R}^m . Therefore, combining them with a generalized linear transformation, as described in Section 3.1, we can now generalize the FC layers:

Poincaré FC layer. Given an input $\mathbf{x} \in \mathbb{B}_c^n$, with the generalized linear transformation v_k in Eq. (7) and the parameters composed of $\mathbf{Z} = \{\mathbf{z}_k \in \mathcal{T}_0 \mathbb{B}_c^n = \mathbb{R}^n\}_{k=1}^m$, which is a generalization of \mathbf{A} and $\mathbf{r} = \{r_k \in \mathbb{R}\}_{k=1}^m$ representing the bias terms, the Poincaré FC layer outputs the following:

$$\mathbf{y} = \mathcal{F}^c(\mathbf{x}; \mathbf{Z}, \mathbf{r}) := \frac{\mathbf{w}}{1 + \sqrt{1 + c\|\mathbf{w}\|^2}} \in \mathbb{B}_c^m, \quad \text{where } \mathbf{w} := \left(\frac{1}{\sqrt{c}} \sinh(\sqrt{c} v_k(\mathbf{x})) \right)_{k=1}^m. \quad (8)$$

It can be confirmed that the signed distance from \mathbf{y} to each Poincaré hyperplane containing the origin, and orthogonal to the k -th axis, equals $v_k(\mathbf{x})$, as proven in Appendix C.3, satisfying the aforementioned properties. We also recover an FC layer in $\lim_{c \rightarrow 0} y_k = 4(\langle \mathbf{a}_k, \mathbf{x} \rangle - r_k \|\mathbf{a}_k\|)$.

Comparison with a previous method. The previously proposed hyperbolic FC layer [9] operates a matrix-vector multiplication in a tangent space and adds a bias through the following Möbius addition: $\mathbf{y} = \exp_0^c(\mathbf{A} \log_0^c(\mathbf{x})) \oplus_c \mathbf{b}$, which indicates that the discriminative hyperplane determined in $\mathcal{T}_0 \mathbb{B}_c^m$ is projected back to \mathbb{B}_c^m by the exponential map at the origin. However, such a surface is no longer a Poincaré hyperplane, except for $\mathbf{b} = \mathbf{0}$. Moreover, the basic shape of the contour surfaces in the output space \mathbb{B}_c^m is determined only by the orientation of each row vector \mathbf{a}_k in \mathbf{A} , whereas their norms and a bias term \mathbf{b} contribute to the total scale and shift. Conversely, the parameters in our method cooperate to realize more various contour surfaces. Notably, discriminative hyperplanes become Poincaré hyperplanes, *i.e.*, the set of all geodesics orthogonal to the orientation \mathbf{z}_k and containing a point $\exp_0^c(r_k [\mathbf{z}_k])$. Therefore, the input space \mathbb{B}_c^n is separated in a more meaningful manner as a hyperbolic space for each k -th dimension of the output space \mathbb{B}_c^m , as shown in Figure 3.

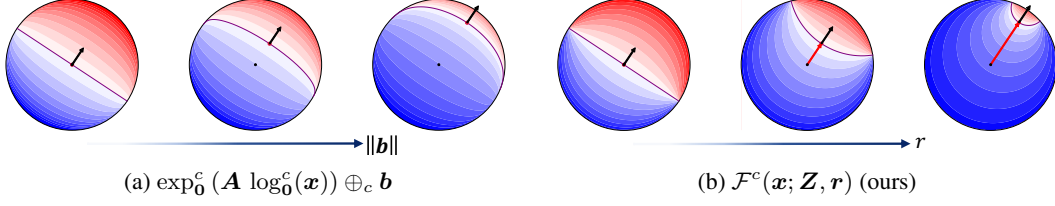


Figure 3: Comparison of FC layers in input spaces \mathbb{B}_c^n . The values at a certain dimension of output spaces are illustrated as contour plots. Black arrows depict the orientation parameters, and they are fixed for the comparison. Their orthogonal curves show discriminative hyperplanes where the values are zeros. As a bias parameter \mathbf{b} or r_k changes, the outline of the contour landscape in (a) remains unchanged, whereas in (b) the focused regions are dynamically squeezed according to the geodesics.

3.3 Split and concatenation

In the Poincaré ball model, merely splitting the coordinates lowers the norms of the output gyrovector, which limits the representational power. In addition, a concatenation of the coordinates is invalid because the norm of the output can easily exceed the domain of the ball. One simple solution is to conduct an operation in the tangent space. The aforementioned problem regarding a split operation, however, remains. Moreover, as the number of inputs to be concatenated increases, the output gyrovector approaches to the boundary of the ball even if the norm of each input is adequately small. The norm of the gyrovector is crucial in the Poincaré ball model owing to its metric. Therefore, reflecting the orientation of inputs while preserving the scale of the norm is considered to be desirable.

Generalization criterion. In Euclidean neural networks, keeping the variance of the feature vectors constant is an essential criterion [13]. As an analogy, keeping the expected values of the norms constant is a worthy criterion in the Poincaré ball model because the norm of any gyrovector in the model is upper-bounded by the ball radius and the variance of the coordinates cannot necessarily remain intact in general when the dimensions in each layer vary. Such a replacement of the statistic invariance target from each coordinate response to the norm is also suggested in [3]. To satisfy this criterion, we propose the following generalization scheme with a scalar coefficient $\beta_n = B(\frac{n}{2}, \frac{1}{2})$.

Poincaré β -split. First, the input $\mathbf{x} \in \mathbb{B}_c^n$ is split in the tangent space with integers $s.t.$ $\sum_{i=1}^N n_i = n$: $\mathbf{x} \mapsto \mathbf{v} = \log_0^c(\mathbf{x}) = (\mathbf{v}_1^\top \in \mathbb{R}^{n_1}, \dots, \mathbf{v}_N^\top \in \mathbb{R}^{n_N})^\top$. Each split tangent vector is then properly scaled and projected back to the Poincaré ball as follows: $\mathbf{v}_i \mapsto \mathbf{y}_i = \exp_0^c(\beta_{n_i} \beta_n^{-1} \mathbf{v}_i)$.

Poincaré β -concatenation. Likewise, the inputs $\{\mathbf{x}_i \in \mathbb{B}_c^{n_i}\}_{i=1}^N$ are first properly scaled and concatenated in the tangent space, and then projected back to the Poincaré ball in the following manner: $\mathbf{x}_i \mapsto \mathbf{v}_i = \log_0^c(\mathbf{x}_i) \in \mathcal{T}_0 \mathbb{B}_c^{n_i}$, $\mathbf{v} := (\beta_n \beta_{n_1}^{-1} \mathbf{v}_1^\top, \dots, \beta_n \beta_{n_N}^{-1} \mathbf{v}_N^\top)^\top \mapsto \mathbf{y} = \exp_0^c(\mathbf{v})$.

We prove the previously mentioned properties under a certain assumption in Appendix C.4. One can also confirm that the Poincaré β -concatenation is the inverse function of the Poincaré β -split.

Discussion about the concatenation. In [9], the concatenation is generalized under the premise that the output is always followed by an FC layer, but such a strong assumption possibly limits its usage. Furthermore, it operates the Möbius addition multiple times, which incurs a heavy computational cost and an unbalanced priority in each input sub-gyrovector. Alternatively, our method with a pair of exponential and logarithmic maps has a lower computational cost and treats every inputs fairly.

3.4 Arbitrary dimensional convolutional layer

The activation of D -dimensional convolutional layers with kernel sizes of $\{K_i\}_{i=1}^D$ is generally described as an affine transformation $y_k = \langle \mathbf{a}_k, \mathbf{x} \rangle - b_k$ for each channel k , where $\mathbf{x} \in \mathbb{R}^{n^K}$ is an input vector per pixel, and is a concatenation of $K = \prod_i K_i$ feature vectors contained in a receptive field of the kernel. This notation also includes a dilated operation. It is now natural to generalize the convolutional layers with Poincaré β -concatenation and a Poincaré FC layer.

Poincaré convolutional layer. At each pixel in the given feature map, the gyrovector $\{\mathbf{x}_s \in \mathbb{B}_c^{n_s}\}_{s=1}^K$ contained in a receptive field of the kernel are concatenated into a single gyrovector $\mathbf{x} \in \mathbb{B}_c^{n^K}$ in the manner proposed in Section 3.3, which is then operated in the same way as a Poincaré FC layer.

3.5 Closed-form centroid in the Poincaré ball model and generalized Möbius coaddition

A centroid is one of the most essential concepts in this field. To generalize the operation for the Poincaré ball model, we utilize the notion of a weighted centroid in the hyperboloid model [19]: With a Lorentzian norm $\|\mathbf{x}\|_{\mathcal{L}} = \sqrt{|\langle \mathbf{x}, \mathbf{x} \rangle_{\mathcal{L}}|} = \sqrt{\|\mathbf{x}\|_{\mathcal{L}}^2}$ for $\mathbf{x} \in \mathbb{R}_1^{n+1}$, the centroid $\bar{\mathbf{h}} \in \mathbb{H}_c^n$ among $\{\mathbf{h}_i \in \mathbb{H}_c^n\}_{i=1}^N$ and non-negative scalar weights $\{\nu_i \in \mathbb{R}_+\}_{i=1}^N$ is given by $\bar{\mathbf{h}} = \underline{\mathbf{h}}(\sqrt{c}\|\underline{\mathbf{h}}\|_{\mathcal{L}})^{-1}$, where $\underline{\mathbf{h}} = \sum_i \nu_i \mathbf{h}_i$ based on the minimization problem of the squared Lorentzian distance $\min_{\bar{\mathbf{h}}} \sum_i \nu_i \|\mathbf{h}_i - \bar{\mathbf{h}}\|_{\mathcal{L}}^2$. We then apply the isometric isomorphism to convert this formulation.

Theorem 1. (*Poincaré weighted centroid*) The centroid $\bar{\mathbf{b}} \in \mathbb{B}_c^n$ that minimizes the sum of squared Lorentzian distances to $\{\mathbf{b}_i \in \mathbb{B}_c^n\}_{i=1}^N$ with the real scalar weights $\{\nu_i \in \mathbb{R}\}_{i=1}^N$ is given by

$$\bar{\mathbf{b}} = \bigoplus_{i=1}^N [\mathbf{b}_i, \nu_i]_c := \frac{\underline{\mathbf{b}}}{1 + \sqrt{1 - c\|\underline{\mathbf{b}}\|^2}}, \quad \text{where } \underline{\mathbf{b}} = 2 \frac{\sum_{i=1}^N \nu_i \frac{\mathbf{b}_i}{1 - c\|\mathbf{b}_i\|^2}}{\sum_{i=1}^N |\nu_i| \frac{1 + c\|\mathbf{b}_i\|^2}{1 - c\|\mathbf{b}_i\|^2}} := \bigoplus_{i=1}^N [\mathbf{b}_i, \nu_i]_c. \quad (9)$$

Note that we extend the condition of the weights to all real values by regarding a negative weight as an additive inverse operation. For more detailed deformation, see Appendix C.5.

Connection to the Möbius coaddition. As a noteworthy property, $\underline{\mathbf{b}}$ can be regarded as a generalization of the Möbius coaddition \boxplus_c , which is a commutative gyrovector addition having duality symmetries with the Möbius addition \oplus_c , as described in Appendix A. This becomes most clear when $N = 2$ and two weights have the same positive values: $\boxplus_{i=1}^2 [\mathbf{b}_i, \nu \in \mathbb{R}_+]_c = \mathbf{b}_1 \boxplus_c \mathbf{b}_2$. The deformation and reasonability of this connection is discussed in Appendix C.6. From this perspective, $\bar{\mathbf{b}}$ can be seen as a regularizer of the norm of summed gyrovector into the averaged gyrovector.

Connection to the Einstein midpoint. As a further encouraging outcome, the Poincaré weighted centroid connects to another type of centroid introduced by Albert Einstein [45]:

Theorem 2. The Poincaré weighted centroid exactly matches the Einstein midpoint defined in the Beltrami-Klein model when the weights all have positive values.

The proof is given in Appendix C.7. Theorems 1 and 2 indicate that these differently motivated hyperbolic centroids can be unified and written in closed-forms in each geometric model.

3.6 Fully hyperbolic multi-head attention in the Poincaré ball model

In this subsection, we describe the construction of a multi-head attention mechanism as a specific example, aiming at a general approach that can be applied to other arbitrary attention schemes.

Multi-head attention. Given a source sequence $\mathbf{S} \in \mathbb{R}^{L_s \times n}$ of length L_s and target sequence $\mathbf{T} \in \mathbb{R}^{L_t \times m}$ of length L_t , the module first projects the target onto query $\mathbf{Q} \in \mathbb{R}^{L_t \times hd}$ and the source onto key $\mathbf{K} \in \mathbb{R}^{L_s \times hd}$ and value $\mathbf{V} \in \mathbb{R}^{L_s \times hd}$ with the corresponding FC layers. These are next split into d -dimensional sub-vectors of h heads and described by superscript i , which is followed by a similarity function between \mathbf{Q}^i and \mathbf{K}^i producing a weight $\mathbf{\Pi}^i = (\pi_{t,s}^i)_{1 \leq t \leq L_t, 1 \leq s \leq L_s} \in \mathbb{R}^{L_t \times L_s}$ applying softmax along the s axis. The weight is utilized to aggregate \mathbf{V}^i into a centroid, giving $\mathbf{X}^i = \mathbf{\Pi}^i \mathbf{V}^i$. Finally, the features in all heads are concatenated into \mathbf{X} and fed to an output FC layer.

Poincaré multi-head attention. We trace almost the same procedures as above. First, the source and target are given as sequences of gyrovector of lengths L_s and L_t , respectively. They are projected with the three Poincaré FC layers, followed by Poincaré β -splits to produce $\mathbf{Q}^i = \{\mathbf{q}_t^i \in \mathbb{B}_c^d\}_{1 \leq t \leq L_t}$, $\mathbf{K}^i = \{\mathbf{k}_s^i \in \mathbb{B}_c^d\}_{1 \leq s \leq L_s}$, and $\mathbf{V}^i = \{\mathbf{v}_s^i \in \mathbb{B}_c^d\}_{1 \leq s \leq L_s}$. As a similarity function, we employ the distance of each query and key, i.e., $\pi_t^i = \text{SoftMax}(\{-\tau^i d^c(\mathbf{q}_t^i, \mathbf{k}_s^i)\}_{s=1}^{L_s})$, where τ^i is the inverse temperature parameter. The values are then aggregated as follows: $\mathbf{x}_t^i = \bigoplus_{s=1}^{L_s} [\mathbf{v}_s^i, \pi_{t,s}^i]_c$. Finally, the features in all heads are Poincaré β -concatenated and fed to an output Poincaré FC layer.

4 Experiments

In the experiments, we evaluate our proposed components and compare them with the previous hyperbolic methods on the Poincaré ball model and original Euclidean architectures. Our implementation of hyperbolic architectures is based on the GeoOpt library [15] built on the PyTorch framework [34].

Table 1: Test F1 scores for four sub-trees of the WordNet noun hierarchy. The first column indicates the number of nodes in each sub-tree for the training and test times. For each setting, we report the 95% confidence intervals for three different trials. Note that the number of parameters of the Euclidean MLR and our approach is $D + 1$, whereas for the hyperbolic MLR in [9], it is $2D$.

RootNode	Model	D=2	D=3	D=5	D=10
animal.n.01 3218 / 798	Unidirectional (ours)	60.69±4.05	67.88±1.18	86.26±4.66	99.15±0.46
	Hyperbolic [9]	59.25±16.88	70.59±1.38	85.89±3.77	99.34±0.39
	Euclidean	39.96±0.89	60.20±0.89	66.20±2.11	98.33±1.12
group.n.01 6649 / 1727	Unidirectional (ours)	74.27±1.50	63.90±6.46	84.36±1.79	85.60±2.75
	Hyperbolic [9]	76.69±1.82	66.79±1.12	84.44±1.88	86.87±1.26
	Euclidean	47.65±0.65	55.15±0.97	71.21±1.81	81.01±1.81
mammal.n.01 953 / 228	Unidirectional (ours)	63.48±3.76	94.98±3.87	99.30±0.30	99.17±1.55
	Hyperbolic [9]	46.96±13.86	95.18±4.19	98.89±1.29	98.75±0.51
	Euclidean	15.78±0.66	36.88±3.83	60.53±3.27	65.63±2.93
location.n.01 2689 / 673	Unidirectional (ours)	42.60±2.69	66.70±2.67	78.18±5.96	92.34±1.84
	Hyperbolic [9]	42.57±5.03	62.21±26.44	77.26±2.02	85.14±2.86
	Euclidean	34.50±0.34	31.44±0.76	63.86±2.18	82.99±3.35

4.1 Verification of the MLR classification capacity

Because the unidirectional Poincaré MLR is the nucleus of our methods, we at first conducted its performance check on the same conditioned experiment designed for the original hyperbolic MLR, that is, a sub-tree classification on the Poincaré ball model. In this task, the Poincaré embeddings [30] of the WordNet [26] noun hierarchy, which contains 82,115 nodes and 743,241 hypernymy relations, are utilized as the data set. We pre-trained the embeddings of two, three, five, and ten dimensions using the open-source implementation¹ of PyTorch, to extract several sub-trees whose root nodes are certain abstract hypernymies, *e.g.*, animal. For each sub-tree, MLR layers learn the binary classification to predict whether each given node is included. As in [9], all nodes are divided into 80% training nodes and 20% testing nodes. We trained a unidirectional Poincaré MLR, a hyperbolic MLR in [9], and an ordinary Euclidean MLR for 30 epochs using Riemannian Adam [3], which acts as Adam for the Euclidean parameters, with a learning rate of 0.001 and a batch size of 16.

The F1 scores for the test sets are shown in Table 1. First, we can confirm the tendency of the hyperbolic MLRs to outperform the Euclidean version in all settings, which illustrates that MLR functions considering the hyperbolic geometry are better suited to the embeddings in a hyperbolic space. Second, we can see that our approach marks the same level of performance as a conventional hyperbolic MLR, but realize in a more stabilized training. We assume that this is due to the parameter efficiency sated in Section 3.1.

4.2 Amortized clustering of Mixture of Gaussians with Set Transformers

We then evaluate a Poincaré multi-head attention because it contains Poincaré FC layers, Poincaré β -split, Poincaré β -concatenation, and Poincaré weighted centroid inside of the module, and is considered to be a proper test case. To eliminate the implicit influence of normalization layers and unessential operations, *e.g.*, positional encoding, we utilize Set Transformer [21], which is composed of various attention mechanisms that can all be converted into layers on the Poincaré ball model using our scheme. According to the official implementation, it does not include normalization layers. The task we evaluated is an amortized clustering of a mixture of Gaussians (MoG). In each sample in a mini batch, models take hundreds of two-dimensional points randomly generated by the same K -components MoG, and estimate all parameters, *i.e.*, the ground truth probabilities, means, and standard deviations, in a single forward step. To allow the hyperbolic models to deal with the values represented in Euclidean coordinates, the inputs and outputs are projected by an exponential map and logarithmic map, respectively. Note that we omit the ReLU activations for the hyperbolic models because the hyperbolic operations are inherently non-linear. The same policy is also mentioned in [9].

¹<https://github.com/facebookresearch/poincare-embeddings>

Table 2: Negative log-likelihood on the test set. Oracle indicates the score when estimating the test sets with the ground truth MoG parameters. For each setting, we report the 95% confidence intervals for all converged results from the five trials. The numbers in brackets indicate the diverged trials.

Model	K=4	K=5	K=6	K=7	K=8
Oracle	1.485	1.675	1.857	2.003	2.132
Set Transformer w/o LN	1.556 ± 0.214 (3)	1.912 ± 0.701 (2)	2.032 ± 0.193 (3)	5.066 ± 5.239 (3)	2.608 $\pm N/A$ (4)
Ours	1.558 ± 0.008 (0)	1.833 ± 0.046 (0)	2.081 ± 0.036 (0)	2.370 ± 0.098 (0)	2.682 ± 0.164 (0)
Set Transformer w/ LN	1.558 ± 0.032 (0)	1.776 ± 0.030 (0)	2.046 ± 0.030 (0)	2.297 ± 0.047 (0)	2.519 ± 0.020 (0)

The results are shown in Table 2. We regard those trials with final scores higher than 10.0 as being diverged, and report the scores calculated only for the converged trials. Comparing with the scores for successful cases, our model achieves equivalent or even better results. Moreover, while the training of Set Transformer often fails under all settings, the training of our approach shows a remarkable stability and consistently converges with the narrow confidence intervals. As a reference, we conducted the experiment of Set Transformer with Layer Normalization, and find that it converges to the slightly better scores than ours. However, in terms of stability, our model achieves almost the same level. This suggests the immanent normalization properties of our hyperbolic architectures, and we ascribe them to the operations taking vector norms as their inputs. It also implies that our model would be further improved with strict normalization layers suitable for the hyperbolic space.

4.3 Convolutional sequence to sequence modeling

Table 3: BLEU-4 scores [33] on newstest2013. The target sentences were decoded using beam search with a beam size of five. D indicates the dimensions of token embeddings and the final MLR layer.

Model	D=16	D=32	D=64	D=128	D=256
ConvSeq2Seq [10]	2.68	8.43	14.92	20.02	21.84
Ours	9.81	14.11	16.95	19.40	21.76

Finally, we confirm the properties of our Poincaré convolutional layers in the task of convolutional sequence to sequence modeling [10] for machine translation of WMT’17 English-German [5]. We follow the open-source implementation of FAIRSEQ [31], where preprocessed training data contains 3.96M sentence pairs with 40K sub-word tokenization in each language. In our hyperbolic models, feature vectors are completely treated as Möbius gyrovectors because token embeddings can be learned directly on the Poincaré ball model. Note that the inputs for the sigmoid functions in Gated Linear Units are logarithmic mapped just as hyperbolic Gated Recurrent Units in [9]. We train various tiny dimensional models to verify the representational capacity of our hyperbolic architectures, with Riemannian Adam for 100K iterations. For more implementation details, please check Appendix D.

The result are shown in Table 3. Our model demonstrates the significant improvements compared to the usual Euclidean models in the fewer dimensions, which reflects the immense embedding capacity of hyperbolic spaces. On the other hand, there is no salient differences observed in higher dimensions, which implies that the Euclidean models with higher dimensions than a certain level can obtain a sufficient computational complexity through the optimization. This would fill the gap with the representational properties of hyperbolic spaces. It also implies that the proper construction of neural networks with the product space of multiple small hyperbolic spaces using our methods have the potential for the further improvements even in higher dimensional architectures.

5 Conclusion

We showed the generalization and construction of the wide variety of neural network architectures in the Poincaré ball model. We achieve this under a unified mathematical backbone based on the concepts of the Riemannian geometry and the Möbius gyrovector space. Through the experiments, we verified the effectiveness of our approaches from diversified perspectives. We hope that this study will pave the way for the future researches in the field of geometric deep learning.

Broader Impact

Because the major focus of this study is to construct the theoretical methodologies to replace a variety of neural network architectures from the perspective of the hyperbolic geometry, it is difficult to state clearly which region our approach could be applicable to. Generally speaking, geometric deep learning that exploits the hyperbolic space has a great potential to deal with a broad range of real-world hierarchical data structures in a proper and efficient manner. We consider that our study contributes to such future applications.

On the other hand, several difficulties exist in applying the deep learning using hyperbolic spaces to the practical deployment. In particular, the operations in the Poincaré ball model generally suffer from the high memory consumption and the slow computational speed compared to the Euclidean counterparts because they must compute and preserve more intermediate variables. Therefore, we consider that the more sophisticated engineering techniques such as CUDA kernels specialized for the hyperbolic geometric computation are required for future practical uses.

Acknowledgments and Disclosure of Funding

We would like to thank Naoyuki Gunji and Yuki Kawana from The University of Tokyo for their helpful discussions. We would also like to thank Editage² and Dr. Lin Gu from RIKEN AIP for proofreading the manuscript for English language.

This work was supported by JST AIP Acceleration Research Grant Number JPMJCR20U3 and JSPS KAKENHI Grant Number JP19H01115, Japan.

References

- [1] Ben Andrews and Christopher Hopper. *The Ricci flow in Riemannian geometry: a complete proof of the differentiable 1/4-pinching sphere theorem*. Springer, 2010.
- [2] Ivana Balazevic, Carl Allen, and Timothy Hospedales. Multi-relational Poincaré Graph Embeddings. In *Advances in Neural Information Processing Systems 32*, pp. 4463–4473. Curran Associates, Inc., 2019.
- [3] Gary Becigneul and Octavian-Eugen Ganea. Riemannian Adaptive Optimization Methods. In *International Conference on Learning Representations*, 2019.
- [4] Thomas Blasius, Tobias Friedrich, Anton Krophmer, Soren Laue, Anton Krophmer, Soren Laue, Tobias Friedrich, and Thomas Blasius. Efficient Embedding of Scale-Free Graphs in the Hyperbolic Plane. *IEEE/ACM Trans. Netw.*, Vol. 26, No. 2, p. 920–933, April 2018.
- [5] Ondrej Bojar, Rajen Chatterjee, Christian Federmann, Yvette Graham, Barry Haddow, Shujian Huang, Matthias Huck, Philipp Koehn, Qun Liu, Varvara Logacheva, Christof Monz, Matteo Negri, Matt Post, Raphael Rubino, Lucia Specia, and Marco Turchi. Findings of the 2017 Conference on Machine Translation (WMT17). In *Proceedings of the Second Conference on Machine Translation, Volume 2: Shared Task Papers*, pp. 169–214, Copenhagen, Denmark, September 2017. Association for Computational Linguistics.
- [6] Ines Chami, Zitao Ying, Christopher Ré, and Jure Leskovec. Hyperbolic Graph Convolutional Neural Networks. In *Advances in Neural Information Processing Systems 32*, pp. 4868–4879. Curran Associates, Inc., 2019.
- [7] Hyunghoon Cho, Benjamin DeMeo, Jian Peng, and Bonnie Berger. Large-Margin Classification in Hyperbolic Space. In *Proceedings of Machine Learning Research*, Vol. 89 of *Proceedings of Machine Learning Research*, pp. 1832–1840. PMLR, 16–18 Apr 2019.
- [8] Octavian-Eugen Ganea, Gary Becigneul, and Thomas Hofmann. Hyperbolic Entailment Cones for Learning Hierarchical Embeddings. In *ICML*, 2018.
- [9] Octavian Ganea, Gary Becigneul, and Thomas Hofmann. Hyperbolic Neural Networks. In *Advances in Neural Information Processing Systems 31*, pp. 5345–5355. Curran Associates, Inc., 2018.
- [10] Jonas Gehring, Michael Auli, David Grangier, Denis Yarats, and Yann N. Dauphin. Convolutional Sequence to Sequence Learning. In Doina Precup and Yee Whye Teh, editors, *Proceedings of the 34th International Conference on Machine Learning*, Vol. 70 of *Proceedings of Machine Learning Research*, pp. 1243–1252, International Convention Centre, Sydney, Australia, 06–11 Aug 2017. PMLR.
- [11] Albert Gu, Frederic Sala, Beliz Gunel, and Christopher Ré. Learning Mixed-Curvature Representations in Product Spaces. In *International Conference on Learning Representations*, 2019.

²<http://www.editage.com>

- [12] Caglar Gulcehre, Misha Denil, Mateusz Malinowski, Ali Razavi, Razvan Pascanu, Karl Moritz Hermann, Peter Battaglia, Victor Bapst, David Raposo, Adam Santoro, and Nando de Freitas. Hyperbolic Attention Networks. *arXiv preprint arXiv:1805.09786*, 2018.
- [13] Kaiming He, Xiangyu Zhang, Shaoqing Ren, and Jian Sun. Delving Deep into Rectifiers: Surpassing Human-Level Performance on ImageNet Classification. In *Proceedings of the IEEE international conference on computer vision*, pp. 1026–1034, 2015.
- [14] Kaoru Katayama and Ernest Weke Maina. Indexing Method for Hierarchical Graphs based on Relation among Interlacing Sequences of Eigenvalues. *Journal of Information Processing*, Vol. 23, No. 2, pp. 210–220, 2015.
- [15] Max Kochurov, Rasul Karimov, and Sergei Kozlukov. Geoopt: Riemannian Optimization in PyTorch. *arXiv preprint arXiv:2005.02819*, 2020.
- [16] Dmitri Krioukov, Fragkiskos Papadopoulos, Maksim Kitsak, Amin Vahdat, and Marián Boguná. Hyperbolic geometry of complex networks. *Physical Review E*, Vol. 82, No. 3, p. 036106, 2010.
- [17] Dmitri Krioukov, Fragkiskos Papadopoulos, Amin Vahdat, and Marián Boguná. Curvature and temperature of complex networks. *Physical Review E*, Vol. 80, No. 3, p. 035101, 2009.
- [18] John Lamping, Ramana Rao, and Peter Pirolli. A Focus+Context Technique Based on Hyperbolic Geometry for Visualizing Large Hierarchies. In *Proceedings of the SIGCHI Conference on Human Factors in Computing Systems*, CHI ’95, pp. 401–408, New York, NY, USA, 1995. ACM Press/Addison-Wesley Publishing Co.
- [19] Marc Law, Renjie Liao, Jake Snell, and Richard Zemel. Lorentzian Distance Learning for Hyperbolic Representations. In *Proceedings of the 36th International Conference on Machine Learning*, Vol. 97 of *Proceedings of Machine Learning Research*, pp. 3672–3681, Long Beach, California, USA, 09–15 Jun 2019. PMLR.
- [20] Guy Lebanon and John Lafferty. Hyperplane Margin Classifiers on the Multinomial Manifold. In *Proceedings of the Twenty-First International Conference on Machine Learning*, ICML ’04, p. 66. Association for Computing Machinery, 2004.
- [21] Juho Lee, Yoonho Lee, Jungtaek Kim, Adam Kosioerek, Seungjin Choi, and Yee Whye Teh. Set Transformer: A Framework for Attention-based Permutation-Invariant Neural Networks. In Kamalika Chaudhuri and Ruslan Salakhutdinov, editors, *Proceedings of the 36th International Conference on Machine Learning*, Vol. 97 of *Proceedings of Machine Learning Research*, pp. 3744–3753, Long Beach, California, USA, 09–15 Jun 2019. PMLR.
- [22] Henry W Lin and Max Tegmark. Critical Behavior in Physics and Probabilistic Formal Languages. *Entropy*, Vol. 19, No. 7, p. 299, 2017.
- [23] Qi Liu, Maximilian Nickel, and Douwe Kiela. Hyperbolic Graph Neural Networks. In *Advances in Neural Information Processing Systems 32*, pp. 8230–8241. Curran Associates, Inc., 2019.
- [24] Emile Mathieu, Charline Le Lan, Chris J. Maddison, Ryota Tomioka, and Yee Whye Teh. Continuous Hierarchical Representations with Poincaré Variational Auto-Encoders. In *Advances in Neural Information Processing Systems 32*, pp. 12565–12576. Curran Associates, Inc., 2019.
- [25] Marko Valentin Micic and Hugo Chu. Hyperbolic Deep Learning for Chinese Natural Language Understanding. *arXiv preprint arXiv:1812.10408*, 2018.
- [26] George A Miller. *WordNet: An Electronic Lexical Database*. MIT press, 1998.
- [27] Yoshihiro Nagano, Shoichiro Yamaguchi, Yasuhiro Fujita, and Masanori Koyama. A Wrapped Normal Distribution on Hyperbolic Space for Gradient-Based Learning. In *ICML*, 2019.
- [28] Mark EJ Newman. Power laws, Pareto distributions and Zipf’s law. *Contemporary physics*, Vol. 46, No. 5, pp. 323–351, 2005.
- [29] Maximilian Nickel and Douwe Kiela. Learning Continuous Hierarchies in the Lorentz Model of Hyperbolic Geometry. In *ICML*, 2018.
- [30] Maximilian Nickel and Douwe Kiela. Poincaré Embeddings for Learning Hierarchical Representations. In *Advances in Neural Information Processing Systems 30*, pp. 6338–6347. Curran Associates, Inc., 2017.
- [31] Myle Ott, Sergey Edunov, Alexei Baevski, Angela Fan, Sam Gross, Nathan Ng, David Grangier, and Michael Auli. FAIRSEQ: A Fast, Extensible Toolkit for Sequence Modeling. In *Proceedings of NAACL-HLT 2019: Demonstrations*, 2019.
- [32] Ivan Ovinnikov. Poincaré Wasserstein Autoencoder. *arXiv preprint arXiv:1901.01427*, 2019.
- [33] Kishore Papineni, Salim Roukos, Todd Ward, and Wei-Jing Zhu. BLEU: a method for automatic evaluation of machine translation. In *Proceedings of the 40th annual meeting on association for computational linguistics*, pp. 311–318. Association for Computational Linguistics, 2002.

- [34] Adam Paszke, Sam Gross, Francisco Massa, Adam Lerer, James Bradbury, Gregory Chanan, Trevor Killeen, Zeming Lin, Natalia Gimelshein, Luca Antiga, Alban Desmaison, Andreas Kopf, Edward Yang, Zachary DeVito, Martin Raison, Alykhan Tejani, Sasank Chilamkurthy, Benoit Steiner, Lu Fang, Junjie Bai, and Soumith Chintala. PyTorch: An Imperative Style, High-Performance Deep Learning Library. In H. Wallach, H. Larochelle, A. Beygelzimer, F. d'Alché-Buc, E. Fox, and R. Garnett, editors, *Advances in Neural Information Processing Systems 32*, pp. 8024–8035. Curran Associates, Inc., 2019.
- [35] Peter Petersen, S Axler, and KA Ribet. *Riemannian Geometry*, Vol. 171. Springer, 2006.
- [36] Frederic Sala, Chris De Sa, Albert Gu, and Christopher Re. Representation Tradeoffs for Hyperbolic Embeddings. In *Proceedings of the 35th International Conference on Machine Learning*, Vol. 80 of *Proceedings of Machine Learning Research*, pp. 4460–4469, Stockholmsmässan, Stockholm Sweden, 10–15 Jul 2018. PMLR.
- [37] Ondrej Skopek, Octavian-Eugen Ganea, and Gary Bécigneul. Mixed-curvature Variational Autoencoders. In *International Conference on Learning Representations*, 2020.
- [38] Michael Spivak. *A Comprehensive Introduction to Differential Geometry*. Publish or Perish, 1979.
- [39] A. Tifrea, G. Becigneul, and O.-E. Ganea. Poincaré GloVe: Hyperbolic Word Embeddings. In *7th International Conference on Learning Representations (ICLR)*, May 2019.
- [40] Abraham Ungar. Gyrovectors Spaces And Their Differential Geometry. *Nonlinear Functional Analysis and Applications*, Vol. 10, , 01 2005.
- [41] Abraham Ungar. Einstein’s Special Relativity: The Hyperbolic Geometric Viewpoint. *PIRT Conference Proceedings*, 02 2013.
- [42] Abraham A Ungar. Hyperbolic Trigonometry and its Application in the Poincaré Ball Model of Hyperbolic Geometry. *Computers & Mathematics with Applications*, Vol. 41, No. 1-2, pp. 135–147, 2001.
- [43] Abraham A Ungar. *Analytic Hyperbolic Geometry and Albert Einstein’s Special Theory of Relativity*. World Scientific, 2008.
- [44] Abraham A Ungar. *Beyond the Einstein Addition Law and its Gyroscopic Thomas precession: The Theory of Gyrogroups and Gyrovectors Spaces*, Vol. 117. Springer Science & Business Media, 2012.
- [45] Abraham Albert Ungar. A Gyrovectors Space Approach to Hyperbolic Geometry. *Synthesis Lectures on Mathematics and Statistics*, Vol. 1, No. 1, pp. 1–194, 2009.

A Möbius gyrovector space

In this section, we briefly introduce the concept of the Möbius gyrovector space, which is a specific type of gyrovector spaces. For a rigorous theoretical and detailed mathematical background of this system, please refer to [40, 45, 42, 44].

A gyrovector space is an algebraic structure that endows the points in a hyperbolic space with vector-like properties based on a special concept called a gyrogroup. This gyrogroup is similar to ordinary vector spaces that provides a Euclidean space with the well-known vector operations based on the notion of groups. As a particular example in physics, this helps to understand the mathematical structure of the Einstein's theory of special relativity where no possible velocity vectors including the sum of velocities in an arbitrary additive order can exceed the speed of light [43, 41]. Because hyperbolic geometry has several isometric models, a gyrovector space also has some variants where the Möbius gyrovector space is a variant for the Poincaré ball model.

As an abstract mathematical system, a gyrovector space is constructed through the following steps: (1) Start from a set G . (2) With a certain binary operation \oplus , create a tuple called a groupoid, or magma (G, \oplus) . (3) Based on five axioms, define a specific type of magma as a gyrogroup. These axioms include several important properties of gyrovector spaces, such as the left gyroassociative law and an operator called a gyrator $\text{gyr} : G \times G \rightarrow \text{Aut}(G, \oplus)$, which generates an automorphism $\text{Aut}(G, \oplus) \ni \text{gyr}[\mathbf{x}, \mathbf{y}] : G \rightarrow G$ given by $z \mapsto \text{gyr}[\mathbf{x}, \mathbf{y}]z$, called a gyration, from two arbitrary points \mathbf{x} and $\mathbf{y} \in G$. The notion of the gyrocommutative law and gyrogroup cooperation are given in this step. (4) Adding ten more axioms related to the statements about a real inner product space and a scalar multiplication \otimes , the gyrovector space (G, \oplus, \otimes) is thus defined.

Some of the important properties of a gyrovector space are listed below. Here, $\mathbf{x}, \mathbf{y}, \mathbf{z} \in G$.

Gyroassociative laws. Although the binary operation \oplus is not necessarily associative in general, it obeys the left gyroassociative law $\mathbf{x} \oplus (\mathbf{y} \oplus \mathbf{z}) = (\mathbf{x} \oplus \mathbf{y}) \oplus \text{gyr}[\mathbf{x}, \mathbf{y}]\mathbf{z}$ and right gyroassociative law $(\mathbf{x} \oplus \mathbf{y}) \oplus \mathbf{z} = \mathbf{x} \oplus (\mathbf{y} \oplus \text{gyr}[\mathbf{y}, \mathbf{x}]\mathbf{z})$. These equations also provide a general closed-form expression of the gyrations: $\text{gyr}[\mathbf{x}, \mathbf{y}]\mathbf{z} = \ominus(\mathbf{x} \oplus \mathbf{y}) \oplus (\mathbf{x} \oplus (\mathbf{y} \oplus \mathbf{z}))$.

Cases in which gyrations become identity maps. If at least one element for gyr is $\mathbf{0} \in G$, the gyrations become an identity map I : $\text{gyr}[\mathbf{x}, \mathbf{0}] = \text{gyr}[\mathbf{0}, \mathbf{x}] = I$. With the loop properties of the gyrations given by $\text{gyr}[\mathbf{x}, \mathbf{y}] = \text{gyr}[\mathbf{x} \oplus \mathbf{y}, \mathbf{y}] = \text{gyr}[\mathbf{x}, \mathbf{y} \oplus \mathbf{x}]$, many other cases can be also derived.

Gyrocommutative law. Although a binary operation \oplus is not necessarily commutative in general, if it obeys the equation $\mathbf{x} \oplus \mathbf{y} = \text{gyr}[\mathbf{x}, \mathbf{y}](\mathbf{y} \oplus \mathbf{x})$, the gyrogroup is called gyrocommutative.

Gyrogroup cooperation. Regarding \oplus as the primal binary addition, the second binary addition in G is defined as the gyrogroup cooperation \boxplus , which is given by $\mathbf{x} \boxplus \mathbf{y} = \mathbf{x} \oplus \text{gyr}[\mathbf{x}, \ominus \mathbf{y}]\mathbf{y}$. This has duality symmetries with the first binary operation \oplus , such that $\mathbf{x} \oplus \mathbf{y} = \mathbf{x} \boxplus \text{gyr}[\mathbf{x}, \mathbf{y}]\mathbf{y}$. In addition, corresponding to the left cancellation law $\ominus \mathbf{x} \oplus (\mathbf{x} \oplus \mathbf{y}) = \mathbf{y}$ inherent in \oplus , the gyrogroup cooperation induces two types of the right cancellation laws: $(\mathbf{x} \oplus \mathbf{y}) \boxminus \mathbf{y} = (\mathbf{x} \boxplus \mathbf{y}) \ominus \mathbf{y} = \mathbf{x}$.

In this formalism, the Möbius gyrovector space is then defined as $(\mathbb{B}_c^n, \oplus_c, \otimes_c)$, where \mathbb{B}_c^n is as previously introduced in Section 2, and \oplus_c and \otimes_c are as shown in the following subsections.

A.1 Möbius addition

In the Möbius gyrovector space, the primary binary operation is denoted as the Möbius addition $\oplus_c : \mathbb{B}_c^n \times \mathbb{B}_c^n \rightarrow \mathbb{B}_c^n$, which is a noncommutative and nonassociative addition, given by the following:

$$\mathbf{x} \oplus_c \mathbf{y} = \frac{(1 + 2c\langle \mathbf{x}, \mathbf{y} \rangle + c\|\mathbf{y}\|^2) \mathbf{x} + (1 - c\|\mathbf{x}\|^2) \mathbf{y}}{1 + 2c\langle \mathbf{x}, \mathbf{y} \rangle + c^2\|\mathbf{x}\|^2\|\mathbf{y}\|^2}, \quad \mathbf{x} \ominus_c \mathbf{y} = \mathbf{x} \oplus_c (-\mathbf{y}). \quad (10)$$

A.2 Möbius Gyrator

The expression of gyrations in the Möbius gyrovector space can be expanded using the equation of the Möbius addition \oplus_c , which is described in [45] as follows:

$$\text{gyr}[\mathbf{x}, \mathbf{y}] : \mathbf{z} \mapsto \mathbf{z} - 2c \frac{(c\langle \mathbf{x}, \mathbf{z} \rangle \|\mathbf{y}\|^2 - \langle \mathbf{y}, \mathbf{z} \rangle (1 + 2c\langle \mathbf{x}, \mathbf{y} \rangle)) \mathbf{x} + (c\langle \mathbf{y}, \mathbf{z} \rangle \|\mathbf{x}\|^2 + \langle \mathbf{x}, \mathbf{z} \rangle) \mathbf{y}}{1 + 2c\langle \mathbf{x}, \mathbf{y} \rangle + c^2\|\mathbf{x}\|^2\|\mathbf{y}\|^2}. \quad (11)$$

By writing down all the special operators \oplus_c for the gyrovectors in \mathbb{B}_c^n into the normal vector operations, the expression of the gyrations can be now seen as a general function for the any real vector $\mathbf{z} \in \mathbb{R}^n$. Indeed, gyrations are extended to invertible linear maps of \mathbb{R}^n in [45].

The Möbius gyrator endows the Möbius gyrovector space with a gyrocommutative nature.

A.3 Möbius coaddition

The gyrogroup cooperation in the Möbius gyrovector space is called the Möbius coaddition, and is given by the following:

$$\mathbf{x} \boxplus_c \mathbf{y} = \mathbf{x} \oplus_c \text{gyr}[\mathbf{x}, \ominus_c \mathbf{y}] \mathbf{y} = \frac{(1 - c\|\mathbf{y}\|^2) \mathbf{x} + (1 - c\|\mathbf{x}\|^2) \mathbf{y}}{1 - c^2\|\mathbf{x}\|^2\|\mathbf{y}\|^2}.$$

With the gamma factor $\gamma_{\mathbf{x}} = (\sqrt{1 - c\|\mathbf{x}\|^2})^{-1}$ for $\mathbf{x} \in \mathbb{B}_c^n$, this is also described in the following manner:

$$\mathbf{x} \boxplus_c \mathbf{y} = \frac{\gamma_{\mathbf{x}}^2 \mathbf{x} + \gamma_{\mathbf{y}}^2 \mathbf{y}}{\gamma_{\mathbf{x}}^2 + \gamma_{\mathbf{y}}^2 - 1}. \quad (12)$$

Note that the Möbius coaddition is not associative but is commutative.

A.4 Möbius scalar multiplication

The Möbius scalar multiplication for $\mathbf{x} \in \mathbb{B}_c^n$ and $r \in \mathbb{R}$ is given by the following:

$$r \otimes_c \mathbf{x} = \frac{1}{\sqrt{c}} \tanh^{-1} \left(r \tanh \left(\sqrt{c} \|\mathbf{x}\| \right) \right) [\mathbf{x}] = \exp_{\mathbf{0}}^c \left(r \log_{\mathbf{0}}^c (\mathbf{x}) \right). \quad (13)$$

In terms of the Riemannian geometry, the Möbius scalar multiplication adjusts the distance of \mathbf{x} from the origin by the scalar multiplier r . The expressions of the logarithmic map $\log_{\mathbf{x}}^c$ and distance in the Möbius gyrovector space are described in the following subsections.

B Poincaré ball model

Owing to the algebraic structure provided by the Möbius gyrovector space, many properties related to the geometry of the Poincaré ball model can be described in implementation-friendly closed-form expressions.

B.1 Exponential and logarithmic maps

The exponential map $\exp_{\mathbf{x}}^c : \mathcal{T}_{\mathbf{x}} \mathbb{B}_c^n \rightarrow \mathbb{B}_c^n$ is described in [9, Lemma 2] as follows:

$$\exp_{\mathbf{x}}^c (\mathbf{v}) = \mathbf{x} \oplus_c \frac{1}{\sqrt{c}} \tanh \left(\frac{\sqrt{c} \lambda_{\mathbf{x}}^c \|\mathbf{v}\|}{2} \right) [\mathbf{v}], \quad \forall \mathbf{x} \in \mathbb{B}_c^n, \mathbf{v} \in \mathcal{T}_{\mathbf{x}} \mathbb{B}_c^n. \quad (14)$$

The logarithmic map $\log_{\mathbf{x}}^c = (\exp_{\mathbf{x}}^c)^{-1} : \mathbb{B}_c^n \rightarrow \mathcal{T}_{\mathbf{x}} \mathbb{B}_c^n$ is also given by the following:

$$\log_{\mathbf{x}}^c (\mathbf{y}) = \frac{2}{\sqrt{c} \lambda_{\mathbf{x}}^c} \tanh^{-1} \left(\sqrt{c} \|\ominus_c \mathbf{x} \oplus_c \mathbf{y}\| \right) [\ominus_c \mathbf{x} \oplus_c \mathbf{y}], \quad \forall \mathbf{x}, \mathbf{y} \in \mathbb{B}_c^n. \quad (15)$$

B.2 Distance

B.2.1 Poincaré distance between two arbitrary points

The distance function d_c is originally and preliminary defined as a binary operation for indicating the distance between two arbitrary points $\mathbf{x}, \mathbf{y} \in \mathbb{B}_c^n$. Based on the notion of the Möbius addition, the distance $d_c : \mathbb{B}_c^n \times \mathbb{B}_c^n \rightarrow \mathbb{R}$ is succinctly described as follows:

$$d_c (\mathbf{x}, \mathbf{y}) = \frac{2}{\sqrt{c}} \tanh^{-1} \left(\sqrt{c} \|\ominus_c \mathbf{x} \oplus_c \mathbf{y}\| \right) = \|\log_{\mathbf{x}}^c (\mathbf{y})\|_{\mathbf{x}}^c. \quad (16)$$

Despite the noncommutative aspect of the Möbius addition \oplus_c , this distance function in Eq. (16) becomes commutative thanks to the commutative aspect of the Euclidean norm of the Möbius addition, which is expressed as follows:

$$\|\mathbf{x} \oplus_c \mathbf{y}\| = \sqrt{\frac{\|\mathbf{x}\|^2 + 2\langle \mathbf{x}, \mathbf{y} \rangle + \|\mathbf{y}\|^2}{1 + 2c\langle \mathbf{x}, \mathbf{y} \rangle + c^2\|\mathbf{x}\|^2\|\mathbf{y}\|^2}}, \quad \forall \mathbf{x}, \mathbf{y} \in \mathbb{B}_c^n. \quad (17)$$

B.2.2 Distance from a point to Poincaré hyperplane

In the Euclidean geometry, the generalized concept of two-dimensional plane to a higher dimensional space \mathbb{R}^n is a hyperplane containing an arbitrary point $\mathbf{p} \in \mathbb{R}^n$ and is the set of all straight lines orthogonal to an arbitrary orientation vector $\mathbf{a} \in \mathbb{R}^n$. Because straight lines in Euclidean spaces are geodesics in terms of the Riemannian geometry, a hyperplane can be generalized as another Riemannian manifold \mathcal{M}^n such that the hyperplane contains an arbitrary point $\mathbf{p} \in \mathcal{M}^n$ and is the set of all geodesics orthogonal to an arbitrary orientation vector at \mathbf{p} , namely, the tangent vector $\mathbf{a} \in \mathcal{T}_{\mathbf{p}}\mathcal{M}^n$. This concept in the Poincaré ball model has been rigorously defined in [9, Definition 3.1] for $\mathbf{p} \in \mathbb{B}_c^n$, $\mathbf{a} \in \mathcal{T}_{\mathbf{p}}\mathbb{B}_c^n$ as follows:

$$\tilde{H}_{\mathbf{a},\mathbf{p}}^c = \{\mathbf{x} \in \mathbb{B}_c^n \mid \langle \log_{\mathbf{p}}^c(\mathbf{x}), \mathbf{a} \rangle_{\mathbf{p}}^c = 0\} = \exp_{\mathbf{p}}^c(\{\mathbf{a}\}^\perp) \quad (18)$$

$$= \{\mathbf{x} \in \mathbb{B}_c^n \mid \langle \ominus_c \mathbf{p} \oplus_c \mathbf{x}, \mathbf{a} \rangle = 0\}. \quad (19)$$

Note that $\{\mathbf{a}\}^\perp$ is the set of all tangent vectors at \mathbf{p} and orthogonal to \mathbf{a} .

In [9], the closed-form description of the distance from a point $\mathbf{x} \in \mathbb{B}_c^n$ to an arbitrary Poincaré hyperplane $\tilde{H}_{\mathbf{a},\mathbf{p}}^c$ has been proven by considering the minimum distance between \mathbf{x} and any point in $\tilde{H}_{\mathbf{a},\mathbf{p}}^c$:

$$d_c(\mathbf{x}, \tilde{H}_{\mathbf{a},\mathbf{p}}^c) := \inf_{\mathbf{w} \in \tilde{H}_{\mathbf{a},\mathbf{p}}^c} d_c(\mathbf{x}, \mathbf{w}) = \frac{1}{\sqrt{c}} \sinh^{-1} \left(\frac{2\sqrt{c}|\langle \ominus_c \mathbf{p} \oplus_c \mathbf{x}, \mathbf{a} \rangle|}{(1 - c\|\ominus_c \mathbf{p} \oplus_c \mathbf{x}\|^2)\|\mathbf{a}\|} \right). \quad (20)$$

B.3 Parallel transport

The concept of a parallel transport is traditionally derived from differential geometry. In the hyperbolic geometry, the gyrovector space provides the algebra to formulate the parallel transport of a gyrovector [44]. When a gyrovector $\ominus_c \mathbf{x} \oplus_c \mathbf{w} \in \mathbb{B}_c^n$ rooted at a point $\mathbf{x} \in \mathbb{B}_c^n$ is transported parallel to another gyrovector $\ominus_c \mathbf{y} \oplus_c \mathbf{z} \in \mathbb{B}_c^n$ rooted at a point $\mathbf{y} \in \mathbb{B}_c^n$ along a geodesic connecting \mathbf{x} and \mathbf{y} , the equation below is satisfied:

$$\ominus_c \mathbf{y} \oplus_c \mathbf{z} = \text{gyr}[\mathbf{y}, \ominus_c \mathbf{x}](\ominus_c \mathbf{x} \oplus_c \mathbf{w}). \quad (21)$$

Because the exponential map in the Poincaré ball model is a bijective function, the parallel transported gyrovector \mathbf{w} and \mathbf{z} can be regarded as the exponential mapped tangent vectors $\mathbf{v} \in \mathcal{T}_{\mathbf{x}}\mathbb{B}_c^n$ rooted at \mathbf{x} and $\mathbf{u} \in \mathcal{T}_{\mathbf{y}}\mathbb{B}_c^n$ rooted at \mathbf{y} , respectively, that is,

$$\ominus_c \mathbf{y} \oplus_c \exp_{\mathbf{y}}^c(\mathbf{u}) = \text{gyr}[\mathbf{y}, \ominus_c \mathbf{x}](\ominus_c \mathbf{x} \oplus_c \exp_{\mathbf{x}}^c(\mathbf{v})). \quad (22)$$

With Eqs. (14) and (15) and the properties of the Möbius gyration described in Appendix A, a succinct expression of the tangent parallel transport $P_{\mathbf{x} \rightarrow \mathbf{y}}^c : \mathcal{T}_{\mathbf{x}}\mathbb{B}_c^n \rightarrow \mathcal{T}_{\mathbf{y}}\mathbb{B}_c^n$ can be obtained as follows:

$$P_{\mathbf{x} \rightarrow \mathbf{y}}^c(\mathbf{v}) := \mathbf{u} = \frac{\lambda_{\mathbf{x}}^c}{\lambda_{\mathbf{y}}^c} \text{gyr}[\mathbf{y}, \ominus_c \mathbf{x}]\mathbf{v}. \quad (23)$$

Note that, in a special case in which $\mathbf{x} = \mathbf{0}$ and $\mathbf{v} \in \mathcal{T}_{\mathbf{0}}\mathbb{B}_c^n$, this equation is simplified as follows:

$$P_{\mathbf{0} \rightarrow \mathbf{y}}^c(\mathbf{v}) = \frac{\lambda_{\mathbf{0}}^c}{\lambda_{\mathbf{y}}^c} \mathbf{v} = (1 - c\|\mathbf{y}\|^2) \mathbf{v}. \quad (24)$$

One can confirm that Eq. (23) deserves to be called a parallel transport in terms of the differential or Riemannian geometry by checking the covariant derivative associated with the Levi-Civita connection of $P_{\mathbf{x} \rightarrow \mathbf{y}}^c$ along a tangent vector field $\dot{\gamma}(t)$ on a smooth curve $\gamma(t)$ from \mathbf{x} to \mathbf{y} vanishes to $\mathbf{0}$.

C Supplemental proofs for proposed methods

C.1 Final deformation of the proposed unidirectional Poincaré MLR

Proof. First, we clarify the relation between the Poincaré hyperplane $\tilde{H}_{a,p}^c$, described in Appendix B.2.2, and the variants $\bar{H}_{a,r}^c$ introduced in Section 3.1:

$$\bar{H}_{a,r}^c = \tilde{H}_{a,q_{a_k,r_k}}^c. \quad (25)$$

We then start the derivation of Eq. (7) from the variables \mathbf{a}_k and \mathbf{q}_{a_k,r_k} described in Section 3.1. Following Eq. (25) and the concept of the distance from a point to a Poincaré hyperplane described in Eq. (20), the generalized MLR score function v_k in Eq. (4) can be written as follows:

$$v_k(\mathbf{x}) = \frac{\lambda_{\mathbf{q}_{a_k,r_k}}^c \|\mathbf{a}_k\|}{\sqrt{c}} \sinh^{-1} \left(\frac{2\sqrt{c} \langle \ominus_c \mathbf{q}_{a_k,r_k} \oplus_c \mathbf{x}, \mathbf{a}_k \rangle}{(1 - c \|\ominus_c \mathbf{q}_{a_k,r_k} \oplus_c \mathbf{x}\|^2) \|\mathbf{a}_k\|} \right), \quad \forall \mathbf{x} \in \mathbb{B}_c^n. \quad (26)$$

With Eq. (17), we obtain

$$\|\ominus_c \mathbf{q}_{a_k,r_k} \oplus_c \mathbf{x}\|^2 = \frac{\|\mathbf{x}\|^2 - 2\langle \mathbf{x}, \mathbf{q}_{a_k,r_k} \rangle + \|\mathbf{q}_{a_k,r_k}\|^2}{1 - 2c\langle \mathbf{x}, \mathbf{q}_{a_k,r_k} \rangle + c^2\|\mathbf{x}\|^2\|\mathbf{q}_{a_k,r_k}\|^2}. \quad (27)$$

Therefore, we can expand the term inside the \sinh^{-1} function in Eq. (26) in the following manner:

$$\begin{aligned} & \frac{2\sqrt{c} \langle \ominus_c \mathbf{q}_{a_k,r_k} \oplus_c \mathbf{x}, \mathbf{a}_k \rangle}{(1 - c \|\ominus_c \mathbf{q}_{a_k,r_k} \oplus_c \mathbf{x}\|^2) \|\mathbf{a}_k\|} \\ &= \frac{2\sqrt{c}}{\|\mathbf{a}_k\|} \frac{- (1 - 2c\langle \mathbf{x}, \mathbf{q}_{a_k,r_k} \rangle + c\|\mathbf{x}\|^2) \langle \mathbf{q}_{a_k,r_k}, \mathbf{a}_k \rangle + (1 - c\|\mathbf{q}_{a_k,r_k}\|^2) \langle \mathbf{x}, \mathbf{a}_k \rangle}{1 - 2c\langle \mathbf{x}, \mathbf{q}_{a_k,r_k} \rangle + c^2\|\mathbf{x}\|^2\|\mathbf{q}_{a_k,r_k}\|^2 - c(\|\mathbf{x}\|^2 - 2\langle \mathbf{x}, \mathbf{q}_{a_k,r_k} \rangle + \|\mathbf{q}_{a_k,r_k}\|^2)} \end{aligned} \quad (28)$$

$$= 2\sqrt{c} \frac{- (1 - 2c\langle \mathbf{x}, \mathbf{q}_{a_k,r_k} \rangle + c\|\mathbf{x}\|^2) \langle \mathbf{q}_{a_k,r_k}, [\mathbf{a}_k] \rangle + (1 - c\|\mathbf{q}_{a_k,r_k}\|^2) \langle \mathbf{x}, [\mathbf{a}_k] \rangle}{1 - c\|\mathbf{q}_{a_k,r_k}\|^2 - c\|\mathbf{x}\|^2 + c^2\|\mathbf{x}\|^2\|\mathbf{q}_{a_k,r_k}\|^2} \quad (29)$$

$$= \frac{2}{1 - c\|\mathbf{x}\|^2} \left(- \frac{\sqrt{c} (1 - 2c\langle \mathbf{x}, \mathbf{q}_{a_k,r_k} \rangle + c\|\mathbf{x}\|^2) \langle \mathbf{q}_{a_k,r_k}, [\mathbf{a}_k] \rangle}{1 - c\|\mathbf{q}_{a_k,r_k}\|^2} + \sqrt{c} \langle \mathbf{x}, [\mathbf{a}_k] \rangle \right). \quad (30)$$

With Eqs. (6) and (14), the term in the outer brackets in Eq. (30) can be further expanded into the form using r_k and \mathbf{z}_k described in Section 3.1:

$$\begin{aligned} & - \frac{\sqrt{c} (1 - 2c\langle \mathbf{x}, \mathbf{q}_{a_k,r_k} \rangle + c\|\mathbf{x}\|^2) \langle \mathbf{q}_{a_k,r_k}, [\mathbf{a}_k] \rangle}{1 - c\|\mathbf{q}_{a_k,r_k}\|^2} + \sqrt{c} \langle \mathbf{x}, [\mathbf{a}_k] \rangle \\ &= - \frac{(1 - 2\sqrt{c} \tanh(\sqrt{c} r_k) \langle \mathbf{x}, [\mathbf{z}_k] \rangle + c\|\mathbf{x}\|^2) \tanh(\sqrt{c} r_k)}{1 - \tanh^2(\sqrt{c} r_k)} + \sqrt{c} \langle \mathbf{x}, [\mathbf{z}_k] \rangle \end{aligned} \quad (31)$$

$$= - (1 + c\|\mathbf{x}\|^2) \sinh(\sqrt{c} r_k) \cosh(\sqrt{c} r_k) + \sqrt{c} \langle \mathbf{x}, [\mathbf{z}_k] \rangle (1 + 2 \sinh^2(\sqrt{c} r_k)) \quad (32)$$

$$= - \frac{1 + c\|\mathbf{x}\|^2}{2} \sinh(2\sqrt{c} r_k) + \sqrt{c} \langle \mathbf{x}, [\mathbf{z}_k] \rangle \cosh(2\sqrt{c} r_k). \quad (33)$$

In addition, we can also expand the term outside the \sinh^{-1} function in Eq. (26) using Eqs. (6) and (14) as follows:

$$\frac{\lambda_{\mathbf{q}_{a_k,r_k}}^c \|\mathbf{a}_k\|}{\sqrt{c}} = \frac{2 \|\mathbf{a}_k\|}{\sqrt{c} (1 - c\|\mathbf{q}_{a_k,r_k}\|^2)} = \frac{2 \|\operatorname{sech}^2(\sqrt{c} r_k) \mathbf{z}_k\|}{\sqrt{c} (1 - \tanh^2(\sqrt{c} r_k))} = \frac{2 \|\mathbf{z}_k\|}{\sqrt{c}}. \quad (34)$$

Combining Eqs. (26), (30), (33), and (34), we finally conclude the proof through the following:

$$v_k(\mathbf{x}) = \frac{2 \|\mathbf{z}_k\|}{\sqrt{c}} \sinh^{-1} \left(\frac{2\sqrt{c} \langle \mathbf{x}, [\mathbf{z}_k] \rangle}{1 - c\|\mathbf{x}\|^2} \cosh(2\sqrt{c} r_k) - \frac{1 + c\|\mathbf{x}\|^2}{1 - c\|\mathbf{x}\|^2} \sinh(2\sqrt{c} r_k) \right). \quad (35)$$

□

C.2 Convergence proof of proposed unidirectional Poincaré MLR to Euclidean MLR

Proof. For the intended proof, we first introduce the following proposition:

Proposition 1. For $x \neq 0$, $\sinh(x)$ over x converges to 1 in the limit $x \rightarrow 0$:

$$\lim_{x \rightarrow 0} \frac{\sinh(x)}{x} = 1. \quad (36)$$

Proof. The result can be obtained based on the definition of the differentiation of a scalar function:

$$\lim_{x \rightarrow 0} \frac{\sinh(x)}{x} = \lim_{x \rightarrow 0} \frac{e^x - e^{-x}}{2x} = \frac{1}{2} \lim_{x \rightarrow 0} \left(\frac{e^x - 1}{x} + \frac{e^{-x} - 1}{-x} \right) \quad (37)$$

$$= \lim_{x \rightarrow 0} \frac{e^x - e^0}{x} = \left. \frac{de^x}{dx} \right|_{x=0} = 1. \quad (38)$$

□

From Proposition 1, we derive the following two propositions.

Proposition 2. For $t \in \mathbb{R}$, $x \neq 0$, $\sinh(tx)$ over x converges to t in the limit $x \rightarrow 0$:

$$\lim_{x \rightarrow 0} \frac{\sinh(tx)}{x} = t. \quad (39)$$

Proof. We divide this proof into two cases:

$$\lim_{x \rightarrow 0} \frac{\sinh(tx)}{x} = \begin{cases} 0 = t & (t = 0) \\ t \lim_{tx \rightarrow 0} \frac{\sinh(tx)}{tx} = t & (t \neq 0, \text{ Proposition 1}) \end{cases}. \quad (40)$$

□

Proposition 3. For $t \in \mathbb{R}$, $x \neq 0$, $\sinh^{-1}(tx)$ over x converges to t in the limit $x \rightarrow 0$:

$$\lim_{x \rightarrow 0} \frac{\sinh^{-1}(tx)}{x} = t. \quad (41)$$

Proof. We can directly utilize Proposition 1 as follows:

$$\lim_{x \rightarrow 0} \frac{\sinh^{-1}(tx)}{x} = \lim_{s \rightarrow 0} \frac{ts}{\sinh(s)} \quad (s = \sinh^{-1}(tx)) \quad (42)$$

$$= t \lim_{s \rightarrow 0} \left(\frac{\sinh(s)}{s} \right)^{-1} = t \quad (\text{Proposition 1}). \quad (43)$$

□

With Propositions 2 and 3, we can now take the limit of Eq. (7) as follows:

$$\begin{aligned} & \lim_{c \rightarrow 0} v_k(\mathbf{x}) \\ &= \lim_{c \rightarrow 0} \frac{2\|\mathbf{z}_k\|}{\sqrt{c}} \sinh^{-1} \left(\frac{2\sqrt{c}\langle \mathbf{x}, [\mathbf{z}_k] \rangle}{1 - c\|\mathbf{x}\|^2} \cosh(2\sqrt{c}r_k) - \frac{1 + c\|\mathbf{x}\|^2}{1 - c\|\mathbf{x}\|^2} \sinh(2\sqrt{c}r_k) \right) \end{aligned} \quad (44)$$

$$= \lim_{c \rightarrow 0} \frac{2\|\mathbf{z}_k\|}{\sqrt{c}} \sinh^{-1} \left(\sqrt{c} \left(\frac{2\langle \mathbf{x}, [\mathbf{z}_k] \rangle}{1 - c\|\mathbf{x}\|^2} \cosh(2\sqrt{c}r_k) - \frac{1 + c\|\mathbf{x}\|^2}{1 - c\|\mathbf{x}\|^2} \frac{\sinh(2\sqrt{c}r_k)}{\sqrt{c}} \right) \right) \quad (45)$$

$$= 2\|\mathbf{z}_k\| (2\langle \mathbf{x}, [\mathbf{z}_k] \rangle - 2r_k) = 4(\langle \mathbf{x}, \mathbf{z}_k \rangle - r_k \|\mathbf{z}_k\|). \quad (46)$$

Moreover, with Eq. (6), we can confirm that \mathbf{z}_k matches \mathbf{a}_k in the limit $c \rightarrow 0$:

$$\lim_{c \rightarrow 0} \mathbf{a}_k = \lim_{c \rightarrow 0} \text{sech}^2(\sqrt{c}r_k) \mathbf{z}_k = \lim_{c \rightarrow 0} \frac{1}{\cosh^2(\sqrt{c}r_k)} \mathbf{z}_k = \mathbf{z}_k. \quad (47)$$

Combining it with Eqs. (3) and (46), we finally conclude the proof as follows:

$$\lim_{c \rightarrow 0} v_k(\mathbf{x}) = 4 (\langle \mathbf{x}, \mathbf{a}_k \rangle - r_k \|\mathbf{a}_k\|) = 4 (\langle \mathbf{a}_k, \mathbf{x} \rangle - b_k), \quad \text{where } b_k := r_k \|\mathbf{a}_k\|. \quad (48)$$

Here, the factor 4 is derived from the squared conformal factor $(\lambda_{\mathbf{x}}^0)^2$ degenerating into a constant value. This corresponds to the fact that the Poincaré ball model \mathbb{B}_c^n converges to the Euclidean space \mathbb{R}^n in the limit $c \rightarrow 0$ except for the same multiplier $\lim_{c \rightarrow 0} (\lambda_{\mathbf{x}}^c)^2 = 4$ owing to its metric tensor. \square

C.3 Proof of the properties of output coordinates of Poincaré FC layer

Proof. To check the properties of the Poincaré FC layer described in Section 3.2, we first clarify the Poincaré hyperplane containing the origin and orthogonal to the k -th axis in \mathbb{B}_c^m . The k -th axis is a geodesic passing through the origin and any point on it except the origin has a non-zero element in only the k -th coordinates. Therefore, an arbitrary point $\mathbf{x} \in \mathbb{B}_c^m$ along the k -th axis can be written as follows:

$$\mathbf{x} = r \mathbf{e}_k, \quad \text{where } \mathbf{e}_k = (\delta_{ik})_{i=1}^m, \quad r \in \left(-\frac{1}{\sqrt{c}}, \frac{1}{\sqrt{c}}\right) \subset \mathbb{R}, \quad (49)$$

which is as intuitive as in a Euclidean space. Specifically, $r = 0$ represents the origin.

We can then easily describe the intended Poincaré hyperplane as follows:

Definition 1. (Poincaré hyperplane containing the origin and orthogonal to the k -th axis)

$$\bar{H}_{\mathbf{e}_k, 0}^c = \{\mathbf{x} = (x_1, x_2, \dots, x_m)^\top \in \mathbb{B}_c^m \mid \langle \mathbf{e}_k, \mathbf{x} \rangle = x_k = 0\}, \quad (50)$$

which is also intuitively obtained.

With Definition 1, the preparation for constructing \mathbf{y} in Eq. (8) is complete.

Derivation of \mathbf{y} . Let $\mathbf{x} \in \mathbb{B}_c^n$ and $\mathbf{y} = (y_1, y_2, \dots, y_m)^\top \in \mathbb{B}_c^m$ be the input and output of the Poincaré FC layer, respectively. Below, we start the proof with the score functions $v_k(\mathbf{x})$ for $\forall k = \{1, 2, \dots, m\}$ already obtained in the same way as in Eq. (7).

To endow \mathbf{y} the properties described in Section 3.2, *i.e.*, the signed distance from \mathbf{y} to each Poincaré hyperplane containing the origin and orthogonal to the k -th axis is equal to $v_k(\mathbf{x})$, we generate a simultaneous equation for $\forall k$ as follows:

$$d_c(\mathbf{y}, \bar{H}_{\mathbf{e}_k, 0}^c) = v_k(\mathbf{x}). \quad (51)$$

With Eqs. (50) and (25) and the notion of the distance from a point to a Poincaré hyperplane described in Eq. (20), these equations are expanded as follows:

$$\frac{1}{\sqrt{c}} \sinh^{-1} \left(\frac{2\sqrt{c} y_k}{1 - c\|\mathbf{y}\|^2} \right) = v_k(\mathbf{x}). \quad (52)$$

Therefore, we obtain the following notation of the coordinates:

$$y_k = \frac{1 - c\|\mathbf{y}\|^2}{2\sqrt{c}} \sinh(\sqrt{c} v_k(\mathbf{x})), \quad \forall k. \quad (53)$$

When considering the Euclidean norm of \mathbf{y} using Eq. (53), the equation for $\|\mathbf{y}\|$ can be derived as follows:

$$\|\mathbf{y}\| = \frac{1 - c\|\mathbf{y}\|^2}{2\sqrt{c}} \sqrt{\sum_{k=1}^m \sinh^2(\sqrt{c} v_k(\mathbf{x}))}. \quad (54)$$

This can be succinctly rewritten as

$$\|\mathbf{y}\| = \frac{1 - c\|\mathbf{y}\|^2}{2} \|\mathbf{w}\|, \quad \text{where } \mathbf{w} = \left(\frac{1}{\sqrt{c}} \sinh(\sqrt{c} v_k(\mathbf{x})) \right)_{k=1}^m. \quad (55)$$

By solving this quadratic equation, the closed form of $\|\mathbf{y}\|$ is obtained through the following:

$$\|\mathbf{y}\| = -\frac{1}{c\|\mathbf{w}\|} + \sqrt{\frac{1}{c^2\|\mathbf{w}\|^2} + \frac{1}{c}}. \quad (56)$$

Substituting Eqs. (55) and (56) for Eq. (53) leads to Eq. (8) in the notation of the coordinates:

$$y_k = \frac{\sqrt{1 + c\|\mathbf{w}\|^2} - 1}{c\|\mathbf{w}\|^2} w_k = \frac{w_k}{1 + \sqrt{1 + c\|\mathbf{w}\|^2}}, \quad \forall k. \quad (57)$$

Confirmation of the existence of \mathbf{y} . Finally, we conclude the proof by checking that \mathbf{y} is always within the domain of the Poincaré ball $\mathbb{B}_c^m = \{\mathbf{y} \in \mathbb{R}^m \mid c\|\mathbf{y}\|^2 < 1\}$:

$$1 - c\|\mathbf{y}\|^2 = \frac{2\left(\sqrt{1 + c\|\mathbf{w}\|^2} - 1\right)}{c\|\mathbf{w}\|^2} > 0. \quad (58)$$

□

C.4 Proof of the properties of the Poincaré β -split and the Poincaré β -concatenation

In this section, we prove the properties of the Poincaré β -split and the Poincaré β -concatenation described in Section 3.3. The Poincaré ball model is different from Euclidean neural networks, on the simple calculation of the expected value and the variance of a particular value related to a feature vector or weight matrix owing to the linearity in their operations. In the Poincaré ball model, calculating such values without any postulate for the probabilistic distribution that the feature gyrovector or tangent vectors follow is difficult owing to the nonlinear transformations in the exponential and logarithmic maps. Thus, we first make the following naive assumption:

Assumption 1. *Each coordinate of an n -dimensional tangent vector in $\mathcal{T}_0\mathbb{B}_c^n$ follows a normal distribution centered at zero with a certain variance $\frac{\sigma_n^2}{c}$.*

The reasons why we assume the distribution on the tangent space rather than on the Poincaré ball model itself are as follows:

1. It is improper to assume a continuous and smooth distribution onto the space with an upper-bounded radius because there must be no probability density on or outside the boundary. The rough idea of discontinuing such probabilities outside the domain of the Poincaré ball and discretely taking only the inside into account seems to lack rationality.
2. One simple way to avoid the above issue is to apply a uniform distribution from zero to the ball radius based on the norm of the gyrovector. However, there is no guarantee that such constancy in the distribution can be realized on a complexly curved geometric structure of the Poincaré ball model.
3. Conversely, a tangent space is a linear space that is attached to the manifold and can be treated as an ordinary vector space.
4. The Poincaré ball model is conformal to the Euclidean space, *i.e.*, preserving the same angles, and at the origin, the gyrovector having the same norms are projected onto the tangent vectors which also have the same norms with their angles unchanged.
5. In Euclidean neural networks, the normal distribution is one of the most popularly considered priors. The multivariate normal distribution is occasionally approximated as an independent and identically distributed distribution for easier calculation.

Because the Poincaré β -split and the Poincaré β -concatenation are inverse functions to each other, it is sufficient to prove the properties of either one of these operations. Here, we show a proof for the Poincaré β -concatenation. Recalling that $\beta_n = B(\frac{n}{2}, \frac{1}{2})$ and considering the following:

Poincaré β -concatenation. The input gyrovector $\{\mathbf{x}_i \in \mathbb{B}_c^{n_i}\}_{i=1}^N$ are first scaled by certain coefficients and concatenated in the tangent space, and then projected back to the Poincaré ball as follows:

$$\mathbf{x}_i \mapsto \mathbf{v}_i = \log_0^c(\mathbf{x}_i) \in \mathcal{T}_0\mathbb{B}_c^{n_i}, \quad \mathbf{v} := \left(\frac{\beta_n}{\beta_{n_1}} \mathbf{v}_1^\top, \dots, \frac{\beta_n}{\beta_{n_N}} \mathbf{v}_N^\top \right)^\top \mapsto \mathbf{y} = \exp_0^c(\mathbf{v}) \in \mathbb{B}_c^n. \quad (59)$$

Proof. At first, we consider the expected value of the norm of each tangent vector \mathbf{v}_i , which is the target of the Poincaré β -concatenation. Because the value $t_i := \frac{c\|\mathbf{v}_i\|^2}{\sigma_{n_i}^2}$ follows a χ^2 distribution based on Assumption 1, the expected value of $\|\mathbf{v}_i\|$ can be obtained as follows:

$$E[\|\mathbf{v}_i\|] = \frac{1}{2^{\frac{n_i}{2}} \Gamma(\frac{n_i}{2})} \int_0^\infty \|\mathbf{v}_i\| e^{-\frac{t_i}{2}} t_i^{\frac{n_i}{2}-1} dt_i \quad (60)$$

$$= \frac{\sigma_{n_i}}{2^{\frac{n_i}{2}} \Gamma\left(\frac{n_i}{2}\right) \sqrt{c}} \int_0^\infty e^{-\frac{t_i}{2} t_i^{\frac{n_i-1}{2}}} dt_i \quad (61)$$

$$= \frac{2^{\frac{n_i+1}{2}} \Gamma\left(\frac{n_i+1}{2}\right) \sigma_{n_i}}{2^{\frac{n_i}{2}} \Gamma\left(\frac{n_i}{2}\right) \sqrt{c}} \quad (62)$$

$$= \sqrt{\frac{2\pi}{c}} \frac{\sigma_{n_i}}{B\left(\frac{n_i}{2}, \frac{1}{2}\right)} \quad (63)$$

$$= \sqrt{\frac{2\pi}{c}} \frac{\sigma_{n_i}}{\beta_{n_i}}. \quad (64)$$

Therefore, when the norm of each input tangent vector \mathbf{v}_i is kept the same by the former part of neural networks before applying this operation, the standard deviation σ_{n_i} must be expressed as follows:

$$\sigma_{n_i} = C\beta_{n_i}, \quad \text{where } C = \text{const.} \quad (65)$$

In addition, using Eq. (59), the squared norm of the Poincaré β -concatenated tangent vector \mathbf{v} is obtained as follows:

$$\|\mathbf{v}\|^2 = \sum_{i=1}^N \left(\frac{\beta_n}{\beta_{n_i}}\right)^2 \|\mathbf{v}_i\|^2 = \sum_{i=1}^N \frac{\beta_n^2}{c} \frac{c \|\mathbf{v}_i\|^2}{\sigma_{n_i}^2} C^2 = \frac{\beta_n^2 C^2}{c} \sum_{i=1}^N t_i. \quad (66)$$

This leads the value $t := \frac{c \|\mathbf{v}\|^2}{\sigma_n^2}$, where $\sigma_n = C\beta_n$, which is expressed as follows:

$$t = \sum_{i=1}^N t_i. \quad (67)$$

Here, t also follows a χ^2 distribution, and the expected value of the norm of \mathbf{v} is obtained as follows:

$$E[\|\mathbf{v}\|] = \frac{1}{2^{\frac{n}{2}} \Gamma\left(\frac{n}{2}\right)} \int_0^\infty \|\mathbf{v}\| e^{-\frac{t}{2} t^{\frac{n}{2}-1}} dt = \sqrt{\frac{2\pi}{c}} \frac{\sigma_n}{\beta_n} = \sqrt{\frac{2\pi}{c}} C, \quad (68)$$

which is the same as the norms of the input tangent vectors. This indicates that each coordinate of \mathbf{v} follows a normal distribution centered at zero with a variance $\frac{\sigma_n^2}{c}$, satisfying the Assumption 1.

Based on the results above, the expected value of the norm of each input gyrovector \mathbf{x}_i is expressed by the following:

$$E[\|\mathbf{x}_i\|] = \int_0^\infty \|\mathbf{x}_i\| \frac{1}{2^{\frac{n_i}{2}} \Gamma\left(\frac{n_i}{2}\right)} e^{-\frac{t_i}{2} t_i^{\frac{n_i-1}{2}}} dt_i \quad (69)$$

$$= \frac{1}{2^{\frac{n_i}{2}} \Gamma\left(\frac{n_i}{2}\right)} \int_0^\infty \frac{1}{\sqrt{c}} \tanh(\sqrt{c} \|\mathbf{v}_i\|) e^{-\frac{t_i}{2} t_i^{\frac{n_i-1}{2}}} dt_i \quad (70)$$

$$= \frac{1}{2^{\frac{n_i}{2}} \Gamma\left(\frac{n_i}{2}\right) \sqrt{c}} \int_0^\infty \tanh(\sigma_{n_i} \sqrt{t_i}) e^{-\frac{t_i}{2} t_i^{\frac{n_i-1}{2}}} dt_i \quad (71)$$

$$= \frac{1}{2^{\frac{n_i}{2}} \Gamma\left(\frac{n_i}{2}\right) \sqrt{c}} \int_0^\infty \sum_{j=1}^\infty \frac{2^{2j} (2^{2j} - 1) B_{2j} (\sigma_{n_i} \sqrt{t_i})^{2j-1}}{(2j)!} e^{-\frac{t_i}{2} t_i^{\frac{n_i-1}{2}}} dt_i \quad (72)$$

$$= \frac{1}{2^{\frac{n_i}{2}} \Gamma\left(\frac{n_i}{2}\right) \sqrt{c}} \sum_{j=1}^\infty \frac{2^{2j} (2^{2j} - 1) B_{2j} \sigma_{n_i}^{2j-1}}{(2j)!} \int_0^\infty e^{-\frac{t_i}{2} t_i^{\frac{n_i-3}{2}+j}} dt_i \quad (73)$$

$$= \frac{1}{2^{\frac{n_i}{2}} \Gamma\left(\frac{n_i}{2}\right) \sqrt{c}} \sum_{j=1}^\infty \frac{2^{2j} (2^{2j} - 1) B_{2j} \sigma_{n_i}^{2j-1}}{(2j)!} 2^{j+\frac{n_i-1}{2}} \Gamma\left(j + \frac{n_i-1}{2}\right) \quad (74)$$

$$= \frac{1}{\sqrt{c}} \sum_{j=1}^\infty \frac{2^{2j} (2^{2j} - 1) B_{2j}}{(2j)!} (\sqrt{2\pi} C)^{2j-1} \frac{\Gamma\left(\frac{n_i}{2}\right)^{2j-2}}{\Gamma\left(\frac{n_i+1}{2}\right)^{2j-1}} \Gamma\left(j + \frac{n_i-1}{2}\right). \quad (75)$$

Note that, for the calculation between Eqs. (71) and (72), we utilize the Taylor series expansion of \tanh for a real value. Furthermore, considering the Laurent series expansion at infinity, we can obtain the following expressions:

$$\Gamma\left(j + \frac{n_i - 1}{2}\right) = (2e)^{-\frac{n_i}{2}} n_i^{j + \frac{n_i}{2}} \left(\frac{2^{\frac{3}{2}-j} \sqrt{\pi}}{n_i} + O\left(\frac{1}{n_i^2}\right) \right), \quad (76)$$

$$\frac{\Gamma\left(\frac{n_i+1}{2}\right)}{\Gamma\left(\frac{n_i}{2}\right)^2} = (2e)^{\frac{n_i}{2}} n_i^{2-\frac{n_i}{2}} \left(\frac{1}{2^{\frac{3}{2}} \sqrt{\pi} n_i} + O\left(\frac{1}{n_i^2}\right) \right). \quad (77)$$

Therefore, in the general cases in which $n_i \gg 1$, we can obtain the following approximation:

$$\frac{\Gamma\left(\frac{n_i}{2}\right)^{2j-2}}{\Gamma\left(\frac{n_i+1}{2}\right)^{2j-1}} \Gamma\left(j + \frac{n_i - 1}{2}\right) = \Gamma\left(j + \frac{n_i - 1}{2}\right) \frac{\Gamma\left(\frac{n_i+1}{2}\right)}{\Gamma\left(\frac{n_i}{2}\right)^2} \left(\frac{\Gamma\left(\frac{n_i}{2}\right)}{\Gamma\left(\frac{n_i+1}{2}\right)} \right)^{2j} \quad (78)$$

$$\simeq (2e)^{\frac{n_i}{2} - \frac{n_i}{2}} \frac{2^{\frac{3}{2}-j} \sqrt{\pi}}{2^{\frac{3}{2}} \sqrt{\pi}} n_i^{j + \frac{n_i}{2} - \frac{n_i}{2} + 2 - 2} \left(\frac{\Gamma\left(\frac{n_i}{2}\right)}{\Gamma\left(\frac{n_i+1}{2}\right)} \right)^{2j} \quad (79)$$

$$= 2^{-j} n_i^j \left(\frac{\Gamma\left(\frac{n_i}{2}\right)}{\Gamma\left(\frac{n_i+1}{2}\right)} \right)^{2j} \quad (80)$$

$$\simeq 2^{-j} n_i^j \left(\frac{\sqrt{\pi} (2e)^{-\frac{n_i}{2}} n_i^{\frac{n_i-1}{2}}}{\sqrt{\pi} (2e)^{-\frac{n_i+1}{2}} (n_i+1)^{\frac{n_i}{2}}} \right)^{2j} \quad (81)$$

$$= 2^{-j} n_i^j \left((2e)^{\frac{1}{2}} \frac{n_i^{\frac{n_i-1}{2}}}{(n_i+1)^{\frac{n_i}{2}}} \right)^{2j} \quad (82)$$

$$= 2^{-j} n_i^j (2e)^j \frac{n_i^{j(n_i-1)}}{(n_i+1)^{jn_i}} \quad (83)$$

$$= e^j \left(\frac{n_i}{n_i+1} \right)^{n_i j} \quad (84)$$

$$\simeq e^j e^{-j} \quad (85)$$

$$= 1. \quad (86)$$

Note that, for the calculation between Eqs. (80) and (81), we utilize Stirling's approximation, *i.e.*, $\Gamma(z) \simeq \sqrt{\frac{2\pi}{z}} \left(\frac{z}{e}\right)^z$. In addition, we utilize the definition of Napier's constant for the approximation between Eqs. (84) and (85), *i.e.*, $\lim_{x \rightarrow \infty} (1 + \frac{1}{x})^x = e$.

Combining Eqs. (75) and (86), the expected value of $\|\mathbf{x}_i\|$ can be approximately expressed by the following:

$$E[\|\mathbf{x}_i\|] \simeq \frac{1}{\sqrt{c}} \sum_{j=1}^{\infty} \frac{2^{2j} (2^{2j} - 1) B_{2j}}{(2j)!} \left(\sqrt{2\pi} C \right)^{2j-1} \quad (87)$$

$$= \frac{1}{\sqrt{c}} \tanh\left(\sqrt{2\pi} C\right) \quad (88)$$

$$= \frac{1}{\sqrt{c}} \tanh\left(\sqrt{c} E[\|\mathbf{v}_i\|]\right). \quad (89)$$

In the same way, the expected value of the Poincaré β -concatenated gyrovector \mathbf{x} is obtained by the following:

$$E[\|\mathbf{x}\|] \simeq \frac{1}{\sqrt{c}} \tanh\left(\sqrt{2\pi} C\right) \quad (90)$$

$$= \frac{1}{\sqrt{c}} \tanh(\sqrt{c} E[\|\mathbf{v}\|]), \quad (91)$$

which concludes the proof. \square

C.5 The deformation of Poincaré weighted centroid

Proof. We start the derivation from the weighted centroid in the hyperboloid model proposed in [19], as previously described in Section 3.5. The center of mass $\bar{\mathbf{h}} \in \mathbb{H}_c^n$ among $\{\mathbf{h}_i = (z_i, \mathbf{k}_i^\top)^\top \in \mathbb{H}_c^n\}_{i=1}^N$ and the non-negative scalar weights $\{\nu_i \in \mathbb{R}_+\}_{i=1}^N$ is given as follows:

$$\bar{\mathbf{h}} = \frac{\underline{\mathbf{h}}}{\sqrt{c} \|\underline{\mathbf{h}}\|_c}, \quad \text{where } \underline{\mathbf{h}} = \sum_{i=1}^N \nu_i \mathbf{h}_i. \quad (92)$$

Expanding this equation with the coordinates, we obtain the following:

$$\bar{\mathbf{h}} = \frac{1}{\sqrt{c}} \frac{\left(\sum_{i=1}^N \nu_i z_i, \sum_{i=1}^N \nu_i \mathbf{k}_i^\top \right)^\top}{\sqrt{\left(\sum_{i=1}^N \nu_i z_i \right)^2 - \left\| \sum_{i=1}^N \nu_i \mathbf{k}_i \right\|^2}}. \quad (93)$$

The point $\bar{\mathbf{b}} \in \mathbb{B}_c^n$, which is a projection of $\bar{\mathbf{h}}$ to the Poincaré ball model using Eq. (1), is expressed in the following manner:

$$\bar{\mathbf{b}} = \frac{1}{\sqrt{c}} \frac{\sum_{i=1}^N \nu_i \mathbf{k}_i}{\sqrt{\left(\sum_{i=1}^N \nu_i z_i \right)^2 - \left\| \sum_{i=1}^N \nu_i \mathbf{k}_i \right\|^2} + \sum_{i=1}^N \nu_i z_i}. \quad (94)$$

Dividing both the numerator and denominator by $\sum_i \nu_i z_i$, this can be rewritten as follows:

$$\bar{\mathbf{b}} = \frac{\underline{\mathbf{b}}}{1 + \sqrt{1 - c \|\underline{\mathbf{b}}\|^2}}, \quad \text{where } \underline{\mathbf{b}} := \frac{1}{\sqrt{c}} \frac{\sum_{i=1}^N \nu_i \mathbf{k}_i}{\sum_{i=1}^N \nu_i z_i}. \quad (95)$$

Next, considering the points $\{\mathbf{b}_i \in \mathbb{B}_c^n\}_{i=1}^N$, which also correspond to $\{\mathbf{h}_i\}_{i=1}^N$, respectively, we can transform the expression of $\underline{\mathbf{b}}$ into an expression with only the coordinates in the Poincaré ball model:

$$\underline{\mathbf{b}} = 2 \frac{\sum_{i=1}^N \nu_i \frac{\mathbf{b}_i}{1 - c \|\mathbf{b}_i\|^2}}{\sum_{i=1}^N \nu_i \frac{1 + c \|\mathbf{b}_i\|^2}{1 - c \|\mathbf{b}_i\|^2}}. \quad (96)$$

Finally, we extend the condition of the weights to all real values $\{\nu_i \in \mathbb{R}\}_{i=1}^N$ by regarding a negative weight as an additive inverse operation, that is, regarding any pair (ν_i, \mathbf{b}_i) as $(|\nu_i|, \text{sign}(\nu_i) \mathbf{b}_i)$:

$$\underline{\mathbf{b}} = 2 \frac{\sum_{i=1}^N \nu_i \frac{\mathbf{b}_i}{1 - c \|\mathbf{b}_i\|^2}}{\sum_{i=1}^N |\nu_i| \frac{1 + c \|\mathbf{b}_i\|^2}{1 - c \|\mathbf{b}_i\|^2}} = \bigoplus_{i=1}^N [\mathbf{b}_i, \nu_i]_c. \quad (97)$$

This concludes the proof. \square

C.6 The reasonability of the generalization of the Möbius coaddition

We previously described that the novel operator $\bigoplus_{i=1}^N [\mathbf{b}_i, \nu_i]_c$ in Eq. (9) for arbitrary points $\{\mathbf{b}_i \in \mathbb{B}_c^n\}_{i=1}^N$ and scalar weights $\{\nu_i \in \mathbb{R}\}_{i=1}^N$ can be contracted into the Möbius coaddition in certain

cases in which there are two operands and the weights have the same positive values, which indicates that two operands are equally summed:

$$\bigoplus_{i=1}^2 [b_i, \nu]_c = 2 \frac{\sum_{i=1}^2 \nu \frac{b_i}{1-c\|b_i\|^2}}{\sum_{i=1}^2 \nu \frac{1+c\|b_i\|^2}{1-c\|b_i\|^2}} = \frac{(1-c\|b_2\|^2)b_1 + (1-c\|b_1\|^2)b_2}{1-c^2\|b_1\|^2\|b_2\|^2} = b_1 \boxplus_c b_2. \quad (98)$$

In this subsection, we show an intuitive way to naturally extend the expression of the Möbius coaddition that also matches our proposed operator.

From Eq. (12), we can expand the equation of the Möbius coaddition such that it can be clearly seen as a commutative binary operation for $b_1, b_2 \in \mathbb{B}_c^n$:

$$b_1 \boxplus_c b_2 = \frac{\gamma_{b_1}^2 b_1 + \gamma_{b_2}^2 b_2}{\gamma_{b_1}^2 + \gamma_{b_2}^2 - 1} = \frac{\sum_{i=1}^2 \gamma_{b_i}^2 b_i}{\sum_{i=1}^2 (\gamma_{b_i}^2 - \frac{1}{2})}. \quad (99)$$

As a commutative multinary operation for $\{b_i \in \mathbb{B}_c^n\}_{i=1}^N$, we can naturally increase the number of additive operands in this equation as follows:

$$\frac{\sum_{i=1}^N \gamma_{b_i}^2 b_i}{\sum_{i=1}^N (\gamma_{b_i}^2 - \frac{1}{2})}. \quad (100)$$

Moreover, introducing scalar weights $\{\nu_i \in \mathbb{R}\}_{i=1}^N$ as the indicators of the dominance of each point b_i to the total summation, and regarding any negative weight as an additive inverse operation, we can further generalize this equation as follows:

$$\frac{\sum_{i=1}^N |\nu_i| \gamma_{b_i}^2 \{\text{sign}(\nu_i) b_i\}}{\sum_{i=1}^N |\nu_i| (\gamma_{\text{sign}(\nu_i) b_i}^2 - \frac{1}{2})} = \frac{\sum_{i=1}^N \nu_i \gamma_{b_i}^2 b_i}{\sum_{i=1}^N |\nu_i| (\gamma_{b_i}^2 - \frac{1}{2})}, \quad (101)$$

which exactly matches our proposed operator as a generalized Möbius coaddition:

$$\frac{\sum_{i=1}^N \nu_i \gamma_{b_i}^2 b_i}{\sum_{i=1}^N |\nu_i| (\gamma_{b_i}^2 - \frac{1}{2})} = \frac{\sum_{i=1}^N \nu_i \frac{b_i}{1-c\|b_i\|^2}}{\frac{1}{2} \sum_{i=1}^N |\nu_i| \frac{1+c\|b_i\|^2}{1-c\|b_i\|^2}} = \bigoplus_{i=1}^N [b_i, \nu_i]_c. \quad (102)$$

C.7 The Poincaré weighted centroid and the Einstein midpoint

In this subsection, we associate the Poincaré weighted centroid with the Einstein midpoint, which is a midpoint operation among multiple points in the Beltrami-Klein model of a hyperbolic geometry.

Beltrami-Klein model. The n -dimensional Beltrami-Klein model of a constant negative curvature $-c$ is defined by $(\mathbb{K}_c^n, \hat{g}^c)$, where $\mathbb{K}_c^n = \{x \in \mathbb{R}^n \mid c\|x\|^2 < 1\}$ and $\hat{g}_x^c = (1-c\|x\|^2)^{-1} \mathbf{I}_n + (1-c\|x\|^2)^{-2} x x^\top$. Here, \mathbb{K}_c^n is an open ball of radius $1/\sqrt{c}$.

Isometric isomorphism. The bijection between an arbitrary point $n \in \mathbb{K}_c^n$ and its unique corresponding point $b \in \mathbb{B}_c^n$, depicted in Figure 4, is given by the following:

$$\mathbb{K}_c^n \rightarrow \mathbb{B}_c^n : \quad b = \frac{n}{1+\sqrt{1-c\|n\|^2}}, \quad (103)$$

$$\mathbb{B}_c^n \rightarrow \mathbb{K}_c^n : \quad n = \frac{2b}{1+c\|b\|^2}. \quad (104)$$

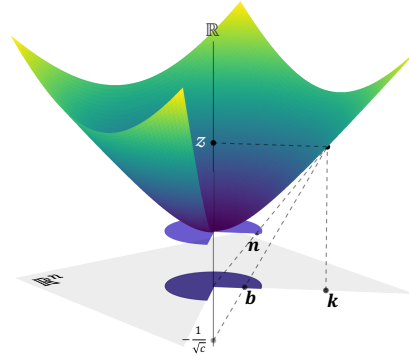


Figure 4: Geometric relationship between $\mathbb{H}_c^n, \mathbb{B}_c^n$ and \mathbb{K}_c^n depicted in \mathbb{R}_1^{n+1} .

Einstein midpoint. In the Beltrami-Klein model, the midpoint $\bar{n} \in \mathbb{K}_c^n$ among $\{n_i \in \mathbb{K}_c^n\}_{i=1}^N$ and the non-negative scalar weights $\{\nu_i \in \mathbb{R}_+\}_{i=1}^N$ is given as follows:

$$\bar{n} = \frac{\sum_{i=1}^N \nu_i \gamma_i n_i}{\sum_{i=1}^N \nu_i \gamma_i}, \quad \text{where } \gamma_i = \frac{1}{\sqrt{1-c\|n_i\|^2}}. \quad (105)$$

This operation is called the Einstein midpoint [45].

Based on the above, we show the proof of Theorem 2.

Proof. Let the points $\{\mathbf{b}_i \in \mathbb{B}_c^n\}_{i=1}^N$ correspond to $\{\mathbf{n}_i \in \mathbb{K}_c^n\}_{i=1}^N$, respectively, i.e., \mathbf{b}_i is a projection of \mathbf{n}_i to the Poincaré ball model using Eq. (103). From Eqs. (104) and (105), we obtain the following:

$$\gamma_i = \frac{1}{\sqrt{1 - c\|\mathbf{n}_i\|^2}} = \frac{1 + c\|\mathbf{b}_i\|^2}{1 - c\|\mathbf{b}_i\|^2}. \quad (106)$$

Substituting Eqs. (103) and (106) for Eq. (105) leads to the representation of the Einstein midpoint using the coordinates in the Poincaré ball model:

$$\bar{\mathbf{n}} = \frac{\sum_{i=1}^N \nu_i \frac{2\mathbf{b}_i}{1 - c\|\mathbf{b}_i\|^2}}{\sum_{i=1}^N \nu_i \frac{1 + c\|\mathbf{b}_i\|^2}{1 - c\|\mathbf{b}_i\|^2}}. \quad (107)$$

Therefore, the point $\bar{\mathbf{b}} \in \mathbb{B}_c^n$, which is a projection of $\bar{\mathbf{n}}$ to the Poincaré ball model using Eq. (103), is expressed in the following manner:

$$\bar{\mathbf{b}} = \frac{\underline{\mathbf{b}}}{1 + \sqrt{1 - c\|\underline{\mathbf{b}}\|^2}}, \quad \text{where } \underline{\mathbf{b}} = \bar{\mathbf{n}} = 2 \frac{\sum_{i=1}^N \nu_i \frac{\mathbf{b}_i}{1 - c\|\mathbf{b}_i\|^2}}{\sum_{i=1}^N \nu_i \frac{1 + c\|\mathbf{b}_i\|^2}{1 - c\|\mathbf{b}_i\|^2}}. \quad (108)$$

This concludes the proof. \square

D Implementation Details

D.1 Parameter initialization

Unidirectional Poincaré MLR. When the dimensions of the input gyrovector is n , each element of the weight parameter \mathbf{Z} is initialized by a normal distribution centered at zero with a standard deviation $n^{-\frac{1}{2}}$. The bias parameter \mathbf{r} is initialized as a zero vector.

Poincaré FC layer. When the dimensions of the input gyrovector and the output gyrovector are n and m , respectively, each element of the weight parameter \mathbf{Z} is initialized by a normal distribution centered at zero with a standard deviation $(2nm)^{-\frac{1}{2}}$. The bias parameter \mathbf{r} is initialized as a zero vector.

Poincaré convolutional layer. When the dimensions of the input gyrovector and the output gyrovector are n and m , respectively, and the total kernel size is K , each element of the weight parameter \mathbf{Z} is initialized by a normal distribution centered at zero with a standard deviation $(2nKm)^{-\frac{1}{2}}$. The bias parameter \mathbf{r} is initialized as a zero vector.

Embedding on the Poincaré ball model. As mentioned in [9], we confirmed the tendency of the parameters in the Poincaré ball model to adjust their angles at the first phase of the training before increasing their norms. In addition, we consider that, due to the exponentially growing distance metric of the hyperbolic space, the farther a gyrovector parameter is placed from the origin, the more costly it moves such a point to another point through the optimization. Therefore, the embedding parameters on the Poincaré ball model should be initialized with a particular small gain ϵ_E , given as a hyperparameter, aiming to accelerate such an adjustment and make the later optimization smooth. We set the value ϵ_E to be 10^{-2} in the experiment in Section 4.3.

D.2 Hyperparameters of the experiment in Section 4.2

Optimization. We used the Riemannian Adam optimizer with $\beta_1 = 0.9$, $\beta_2 = 0.999$ and $\epsilon = 10^{-8}$ for both of the Euclidean and our hyperbolic architectures. The learning rate η was set to 10^{-3} .

D.3 Hyperparameters of the experiment in Section 4.3

Model architectures. Let D be the dimension of the source and target token embeddings. Each model for the experiment in Section 4.3 has the encoder and decoder, both of which are composed of five convolutional layers with a kernel size of three and a channel size of D , five convolutional layers with a kernel size of three and a channel size of $2D$, and two convolutional layers with a kernel size of one and a channel size of $4D$. The output feature maps of the last convolutional layer in the encoder are projected into D -dimensional feature maps. They are utilized as the key for the encoder-decoder attentions. Likewise, the output feature maps of the last convolutional layer in the decoder are projected into D -dimensional feature maps for the final token classification.

Training. In each iteration of the training phase, we fed each model a mini-batch containing approximately 10,000 tokens at most. In this setting, the batch size, or the number of the sentence pairs in a mini-batch, dynamically changes.

As a loss function, we utilized the cross entropy function with a label smoothing of 0.1.

Optimization. We used the Riemannian Adam optimizer with $\beta_1 = 0.9$, $\beta_2 = 0.98$ and $\epsilon = 10^{-9}$ for both of the Euclidean and our hyperbolic architectures. For the scheduling of the learning rate η , we linearly increased the learning rate for the first 1000 iterations as a warm-up, and utilized the inverse square root decay with respect to the number of iterations t thereafter as $\eta = (Dt)^{-\frac{1}{2}}$.